

# Building a Better Li-Garnet Solid Electrolyte/Metallic Li Interface with Antimony

Romain Dubey, Jordi Sastre, Claudia Cancellieri, Faruk Okur, Alexander Forster, Lea Pompizii, Agnieszka Priebe, Yaroslav E. Romanyuk, Lars P. H. Jeurgens, Maksym V. Kovalenko,\* and Kostiantyn V. Kravchyk\*

The deployment of Li-garnet  $\text{Li}_7\text{La}_3\text{Zr}_2\text{O}_{12}$  (LLZO) solid-state electrolytes in solid-state batteries is severely hampered by their poor wettability with metallic Li. In this work, Sb is presented as a compelling interfacial layer allowing superior wetting of Li onto a LLZO surface, resulting in a remarkably low Li/LLZO interfacial resistance of  $4.1(1) \Omega \text{ cm}^2$ . An atomistic insight into Sb-coated LLZO interface using soft and hard X-ray photoelectron spectroscopy and focused ion beam time-of-flight secondary ion mass spectrometry shows the formation of a Li-Sb alloy as an interlayer. It is determined that the Li/Sb-coated LLZO/Li symmetrical cells exhibit a high critical current density of up to  $0.64 \text{ mA cm}^{-2}$  and low overpotentials of 40–50 mV at a current density of  $0.2 \text{ mA cm}^{-2}$  without applying external pressure. The electrochemical performance of Sb coated-LLZO pellets is also assessed with an intercalation-type  $\text{V}_2\text{O}_5$  cathode. Li/Sb-coated-LLZO/ $\text{V}_2\text{O}_5$  full cells deliver stable capacities of around  $0.45 \text{ mAh cm}^{-2}$ , with a peak current density of  $0.3 \text{ mA cm}^{-2}$ .

## 1. Introduction

The quest for safe, non-flammable, and temperature-tolerant energy storage systems with high energy and power densities has caused a surge of research on batteries that consist solely of solid-state components.<sup>[1,2]</sup> In particular, solid-state batteries (SSBs) employing cubic  $\text{Li}_7\text{La}_3\text{Zr}_2\text{O}_{12}$  (LLZO) garnet-type solid electrolytes are appealing as energy storage technology,<sup>[3]</sup> owing to a superior set of properties, such as a high Li-ion conductivity of up to  $1 \text{ mS cm}^{-1}$  (RT), a low electronic conductivity of  $\approx 10^{-8} \text{ S cm}^{-1}$  (RT), a high thermal and mechanical stability and a wide electrochemical operation window of 0–6 V versus  $\text{Li}^+/\text{Li}$ .<sup>[4,5]</sup> LLZO-based SSBs, nevertheless, still face a number of obstacles before they can be practically deployed.<sup>[6]</sup> One of the fore-

most issues is the poor LLZO wettability by lithium metal,<sup>[7]</sup> mainly caused by the presence of the Li-ion-insulating layer at the LLZO surface, composed of LiOH, and  $\text{Li}_2\text{CO}_3$ ,<sup>[8,9]</sup> although some differences as to its thickness and constituents have been reported.<sup>[10–12]</sup> The presence of this surface layer has decisive implications on the electrochemical performance of LLZO-SSBs. At best, this leads to an increase in the Li/LLZO interfacial resistance<sup>[10,11]</sup> and, consequently, to high voltage polarization upon Li plating/stripping.<sup>[13]</sup> At worst, it results in the formation of Li dendrites induced by the inhomogeneous distribution of the applied current density (current focusing).<sup>[4]</sup>

Towards solving the issue of poor LLZO wettability by lithium metal, various approaches of LLZO surface treatment were extensively explored. For instance, conventional heat treatments of LLZO at 600–900 °C<sup>[14]</sup> and surface treatments by HCl,<sup>[15]</sup>  $\text{LiBF}_4$  in ACN<sup>[16]</sup> have been shown to be effective in removing thin Li-ion insulating surface layers. Additionally, employment of  $\text{Al}_2\text{O}_3$ ,<sup>[7]</sup> Au,<sup>[17]</sup>  $\text{SnO}_2$ ,<sup>[18]</sup> graphite,<sup>[19]</sup> Mg,<sup>[20]</sup> Ge<sup>[21]</sup> as interlayers between LLZO and Li reduces the Li/LLZO interfacial resistance (a recent overview is provided by Kim et al.<sup>[2]</sup>). This effect was chiefly attributed to the reaction between these interlayer materials and Li, forming Li-ion conducting compounds.

We have chosen to examine Sb as an interfacial layer, inspired by the prior art with Ge,<sup>[21]</sup> Si,<sup>[22]</sup> and Sn.<sup>[23]</sup> A common motif here is that these elements form alloys with Li. We

R. Dubey, F. Okur, A. Forster, L. Pompizii, M. V. Kovalenko, K. V. Kravchyk  
Laboratory of Inorganic Chemistry  
Department of Chemistry and Applied Biosciences  
ETH Zürich  
Zürich CH-8093, Switzerland

E-mail: mvkovalenko@ethz.ch; kravchyk@inorg.chem.ethz.ch

R. Dubey, J. Sastre, F. Okur, A. Forster, L. Pompizii, Y. E. Romanyuk,  
M. V. Kovalenko, K. V. Kravchyk  
Laboratory for Thin Films and Photovoltaics  
Empa-Swiss Federal Laboratories for Materials Science & Technology  
Dübendorf CH-8600, Switzerland

C. Cancellieri, L. P. H. Jeurgens  
Laboratory for Joining Technologies & Corrosion  
Empa-Swiss Federal Laboratories for Materials Science & Technology  
Dübendorf CH-8600, Switzerland

A. Priebe  
Laboratory for Mechanics of Materials and Nanostructures  
Empa-Swiss Federal Laboratories for Materials Science and Technology  
Feuerwerkerstrasse 39, Thun CH-3602, Switzerland

 The ORCID identification number(s) for the author(s) of this article can be found under <https://doi.org/10.1002/aenm.202102086>.

© 2021 The Authors. Advanced Energy Materials published by Wiley-VCH GmbH. This is an open access article under the terms of the Creative Commons Attribution-NonCommercial License, which permits use, distribution and reproduction in any medium, provided the original work is properly cited and is not used for commercial purposes.

DOI: 10.1002/aenm.202102086

demonstrate that a thin film of Sb on the LLZO surface serves as a wetting layer for Li deposition, yielding low interfacial resistance of  $4.1(1) \Omega \text{ cm}^2$ , and a high critical current density of Li plating/stripping of  $\approx 0.64 \text{ mA cm}^{-2}$ . The Li/Sb-coated LLZO interface has been studied by soft and hard X-ray photoelectron spectroscopy (XPS/HAXPES), and focused ion beam time-of-flight secondary ion mass spectroscopy (FIB-TOF-SIMS).

## 2. Results and Discussion

### 2.1. The Preparation of a Sb-Coated LLZO Solid-State Electrolyte

LLZO solid-state electrolyte with a nominal composition of  $\text{Li}_{6.25}\text{Al}_{0.25}\text{La}_3\text{Zr}_2\text{O}_{12}$  was prepared in the form of highly dense (95–98% of the theoretical density of  $5.17 \text{ g cm}^{-3}$ ) sintered pellets with a thickness of  $\approx 1 \text{ mm}$  and a diameter of  $\approx 10 \text{ mm}$  (see Methods section for details). Then the pellets were polished with SiC paper (grain size 320, then 1000) under air, followed by a heat-treatment at  $600 \text{ }^\circ\text{C}$  for 1 h in an Ar-filled glovebox. The powder X-ray diffraction measurements (Figure 1a) confirmed the formation of a phase-pure cubic LLZO structure (Figure 1b, the space group,  $\text{Ia}\bar{3}\text{d}$ ,  $a = 12.9652(4) \text{ \AA}$ ,  $V = 2179.404 \text{ \AA}^3$ , ICSD 430 571).

Sb thin films were coated via magnetron sputtering onto heat-treated LLZO pellets under an argon atmosphere using an Sb target. Scanning electron microscopy (SEM) measurements

with energy dispersive x-ray analysis of an Sb-coated LLZO pellet revealed that Sb was uniformly distributed throughout the LLZO circular planar surface (Figure 1c). The resulting surface of the LLZO pellets has a shiny, grayish color (Figure 1d). Interestingly, the color turns to shiny orange within seconds after being in contact with molten Li (Figure 1e), indicating the formation of another compound. As foreseen, Sb-coated LLZO pellets demonstrated improved wettability with molten Li, resulting in a low Li/LLZO contact angle (Figure 1f). By contrast, uncoated LLZO pellets exhibited a lithiophobic behavior, refusing any close contact with molten Li, as shown in Figure 1g.

Aiming to determine the optimal thickness of the Sb interfacial layer, double-side Sb-coated LLZO pellets with different Sb thicknesses ranging from 5 to 100 nm were analyzed by impedance spectroscopy. The thickness error was  $\approx 9.5\%$  (see Figure S1 in the Supporting Information). Before the measurements, a  $\approx 50 \mu\text{m}$  thick Li foil (6 mm diameter) was isostatically pressed onto the Sb surface and then heat-treated at  $220 \text{ }^\circ\text{C}$  on a hot plate under inert conditions. Figure 2 compares the electrochemical impedance spectra obtained with different thicknesses of the Sb interfacial layer. The first and second semi-circles are attributed to the total resistance of LLZO pellet and the Li/LLZO interfacial resistance, according to previous reports on LLZO solid-state electrolytes.<sup>[10]</sup> The total ionic conductivity of the LLZO pellets was between  $0.45$  and  $0.5 \text{ mS cm}^{-1}$ . A comparison of the impedance spectra shows that reducing the Sb

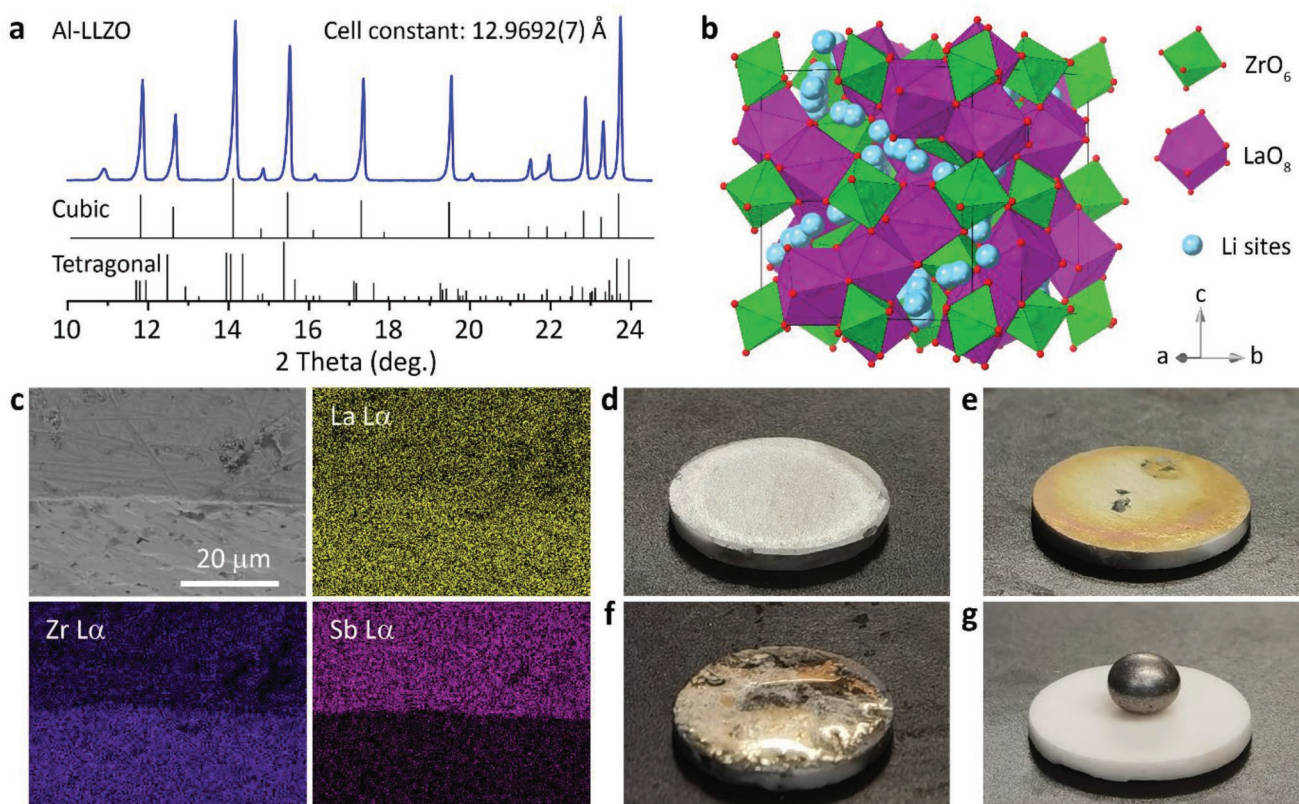


**Figure 1.** a) Powder X-ray diffraction pattern (XRD) of a LLZO pellet after sintering. b) The cubic structure of LLZO along with the representation of possible Li-ion migration pathways as proposed by Junji et al.<sup>[24]</sup> and Chen et al.<sup>[25]</sup> c) SEM-EDX images of Sb-coated LLZO pellet. d–g) Optical images of d) as prepared Sb-coated LLZO pellet, e) Sb-coated LLZO pellet after short contact with molten Li, f) Sb-coated LLZO pellet wetted by molten Li, and g) uncoated LLZO pellets with molten Li.

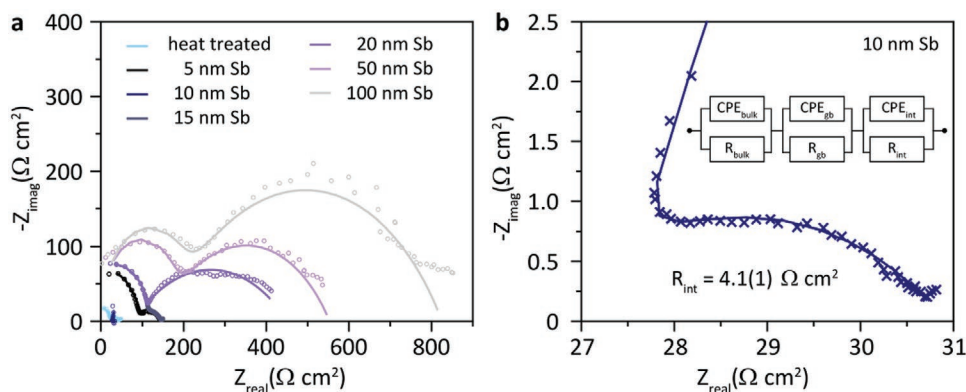


**Figure 2.** a) Impedance spectra of Li/LLZO/Li symmetrical cells comprising Sb-coated LLZO pellets with different Sb thicknesses. An impedance spectrum of heat-treated LLZO without Sb interfacial layer is included for comparison. b) Zoom-in version of the impedance spectrum of the Li/LLZO/Li symmetrical cell comprising 10 nm Sb-coated LLZO pellet. The Li/LLZO interfacial resistance values derived from the impedance spectra are shown in Table S1 in the Supporting Information.

thickness from 100 to 10 nm leads to a decrease in the interfacial resistance from 660(20) to 4.1(1)  $\Omega \text{ cm}^2$ . Interestingly, a further reduction of the thickness up to 5 nm results in an increase of the interfacial resistance to 59(3)  $\Omega \text{ cm}^2$ . Of note, the best symmetrical cell made of heat-treated LLZO without Sb interfacial layer has an interfacial resistance of 28.2(1.4)  $\Omega \text{ cm}^2$  (Figure S2, Supporting Information), which is comparable to the majority of reported values of Li/heat-treated LLZO interface.<sup>[13]</sup>

## 2.2. Surface Characterization

Next, we systematically investigated the surface chemistry of LLZO pellets after each successive preparation step by X-ray photoelectron spectroscopy (XPS). The LLZO pellets were examined before and after heat-treatment (600 °C for 1 h under inert conditions). Additionally, a heat-treated LLZO pellet was measured after two Ar sputter-cleaning cycles at 1 kV (sputter area of  $2 \times 2 \text{ mm}^2$ ), which corresponds to approximate sputter depths of  $\approx 10$  and  $\approx 20$  nm, respectively (as estimated from the calibrated sputter-rate of  $2.3 \text{ nm min}^{-1}$  for a reference  $\text{Ta}_2\text{O}_5$  film). In Figure 3a, the measured La  $3d_{5/2}$ , O 1s, C 1s, and Li 1s spectra of the non-heat-treated, pristine sample after polishing are depicted. The probing depths for the La 3d, O 1s, C 1s, and Li 1s photoelectron lines, as recorded from LLZO using Al-K $\alpha$  X-ray radiation ( $h\nu = 1486.7 \text{ eV}$ ), equal 3.6, 4.8, 5.5, and 6.6 nm, respectively (see Supporting Information for formalism about probing depths). The XPS analysis indicates the presence of a thick overlayer, which is mainly constituted of  $\text{Li}_2\text{CO}_3$  (with traces of Na).

The resolved O 1s, C 1s and Li 1s main peaks at binding energy (BE) values of  $530.1 \pm 0.4 \text{ eV}$ ,  $288.4 \pm 0.4 \text{ eV}$  and  $53.6 \pm 0.4 \text{ eV}$  are assigned to  $\text{Li}_2\text{CO}_3$ ,<sup>[14]</sup> whereas the smaller C 1s peak at  $283.4 \pm 0.4 \text{ eV}$  is attributed to adventitious carbon (see Supporting Information for comments about charge neutralization/referencing). The substrate signals from La (and Zr) are only very weak, which suggests that the polishing step under shielding gas with short air exposure, introduces a heterogeneous  $\text{Li}_2\text{CO}_3$  overlayer with an average thickness of several nanometers. The  $\text{Li}_2\text{CO}_3$  overlayer has formed due to the reaction of Li from LLZO with moist air<sup>[9,10]</sup> and/or carbon residues during the polishing step.

In Figure 3b, the measured La  $3d_{5/2}$ , O 1s, C 1s, and Li 1s spectra of the heat-treated sample are shown. The heat-treatment, as well as the transport of the heat-treated sample for XPS analysis, were performed under a shielding atmosphere. As such, the air-exposure of the heat-treated (during transfer of the sample into the UHV chamber of the XPS instrument) could be minimized to  $< 30$  s. Nonetheless, the substrate signals from La and Zr in the LLZO lattice are still relatively small, which indicates the presence of an overlayer on the heat-treated LLZO substrate. However, the O 1s and C 1s spectral contributions from  $\text{Li}_2\text{CO}_3$  are much lower as compared to the polished, non-heat-treated sample. The O 1s spectral contribution from  $\text{Li}_2\text{CO}_3$  (at  $530.1 \pm 0.4 \text{ eV}$ ) is relatively small; two additional O 1s spectral contributions were resolved, as attributed to  $\text{Li}_2\text{O}/\text{LiOH}$  at  $529.7 \pm 0.4 \text{ eV}$  and oxygen in the LLZO lattice ( $\text{O}_{\text{Lattice}}$ ) at  $527.0 \pm 0.4 \text{ eV}$ .<sup>[26]</sup> The C 1s spectrum also evidences a much lower  $\text{Li}_2\text{CO}_3$  surface content as compared to the non-heat-treated sample (compare C 1s spectra in Figure 3a,b). Unfortunately, the chemical shifts of the Li 1s photoelectron lines between the individual  $\text{O}_{\text{Lattice}}$ ,  $\text{Li}_2\text{O}$ ,  $\text{Li}_2\text{O}_2$ , and  $\text{LiOH}$  chemical species are relatively small (as compared to their respective intrinsic peak widths) and their spectral contributions overlap with the Zr 4s peak from LLZO (see last column in Figure 3). Moreover, differential charging of the insulating LLZO surface will be slightly different depending on the composition of the overlayer. Hence, the individual Li 1s spectral contributions from  $\text{Li}_2\text{CO}_3$ ,  $\text{Li}_2\text{O}$  and/or  $\text{LiOH}$  cannot be resolved unambiguously. Therefore, only a single Li 1s spectral contribution for  $\text{Li}_2\text{CO}_3$ ,  $\text{Li}_2\text{O}$ ,  $\text{LiOH}$  and/or Li in the LLZO lattice (plus a Zr 4s peak from Zr in the LLZO lattice) is fitted in this study. Nonetheless, the XPS analysis clearly evidences that the overlayer on heat-treated LLZO is much thinner as compared to the non-heat-treated sample and constituted of a mixture of  $\text{Li}_2\text{CO}_3$ ,  $\text{Li}_2\text{O}$  and  $\text{LiOH}$  (with traces of Na and F). As follows from the Figure 3c,d, short sputter-cleaning successively removes the  $\text{Li}_2\text{CO}_3/\text{Li}_2\text{O}/\text{LiOH}$  overlayer, resulting in increased signal intensities from La, O, and Li in the LLZO lattice, practically free from surface contaminants. The respective Li 1s peak shifts from predominantly  $\text{Li}_2\text{CO}_3$  at  $53.6 \pm 0.4 \text{ eV}$  to prevailing Li in the LLZO lattice at  $53.2 \text{ eV} \pm 0.4 \text{ eV}$ . The drastic reduction of the  $\text{Li}_2\text{CO}_3$  surface

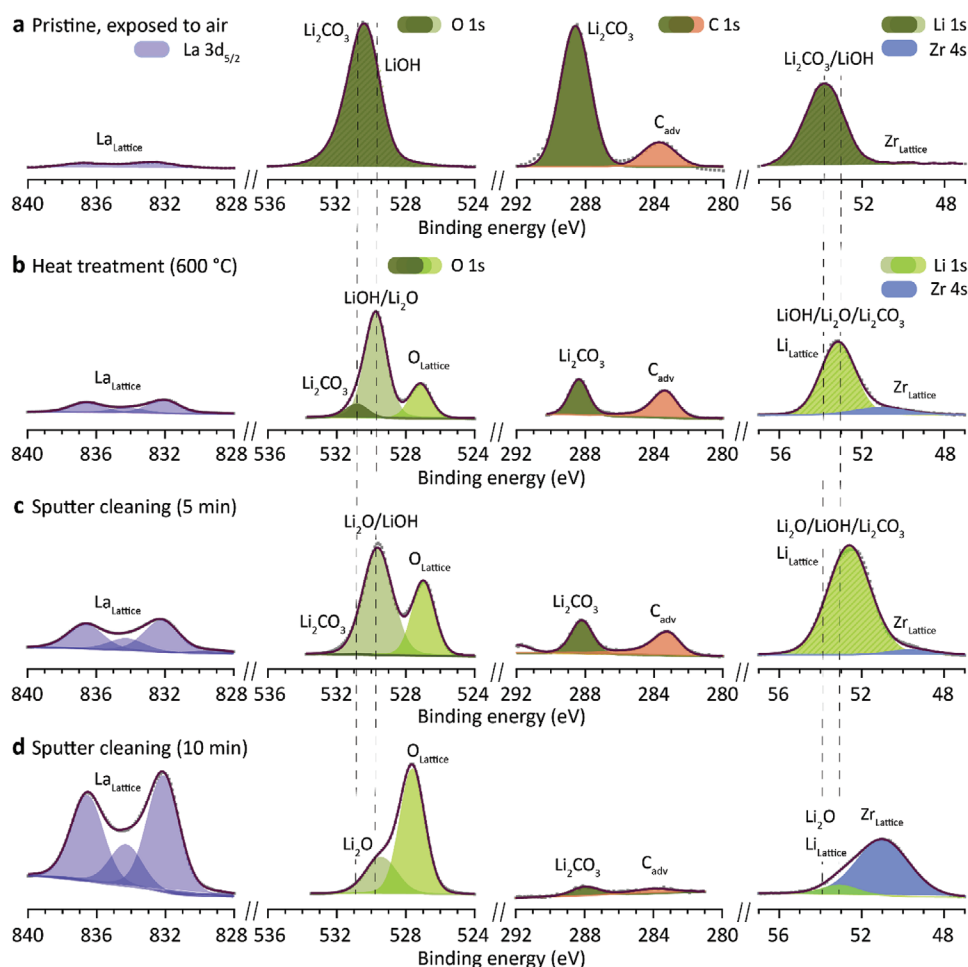


**Figure 3.** La  $3d_{5/2}$ , O 1s, C 1s, and Li 1s XPS spectra of a LLZO surface. a) After polishing in air without further heat treatment, b) after heat treatment ( $600\text{ }^{\circ}\text{C}$ , 1 h, under Ar) and a brief exposure to air ( $< 30\text{ s}$ ), c) after sputter cleaning (5 min, depth of  $\approx 10\text{ nm}$ ), and d) after sputter cleaning (10 min, depth of  $\approx 20\text{ nm}$ ) of the LLZO surface pertaining to (a). Here it is noted that the spectra referring to (a) were measured at a higher pass energy, resulting in a lower energy resolution (i.e., broader peaks).

content is a direct consequence of the applied heat treatment, as expected.

These results highlight the extreme sensitivity of the LLZO surface to moisture and air. A heat-treatment of the polished LLZO surface is needed to reduce the overlayer of surface contaminants, thus creating a much cleaner surface for successive deposition of Sb and/or Li (see what follows). These results are in line with previously published LLZO studies. However, the depth-dependent chemical constitution of the reaction layer remains unclear, since sputter cleaning is a destructive technique which affect the chemical states by sputter artifacts, such as preferential sputtering, ion-bombardment induced mixing and surface roughening. Therefore, in this study, a more detailed analysis of the surface overlayer by lab-based hard X-ray spectroscopy XPS (HAXPES) was performed, which opens unique opportunities to investigate the unperturbed chemical constitution of the reaction layer up to much larger probing depths.

The probing depth by Cr X-rays is about three times deeper than the respective probing depth using Al X-rays. The calculated probing depths for the La 3d, O 1s, C 1s, and Li 1s

photoelectron lines, as recorded from LLZO using Cr- $K\alpha$  X-ray radiation ( $h\nu = 514.7\text{ eV}$ ), equal 16.9, 176, 18.3, and 19.2 nm, respectively. The conventional XPS measurements with soft Al- $K\alpha$  X-rays on the heat-treated sample, as displayed in Figure 3, were repeated by HAXPES using hard Cr- $K\alpha$  X-rays on the identical analysis area of the same sample: see Figure 4. Strikingly, no carbon species (from  $\text{Li}_2\text{CO}_3$  or adventitious C) are detected by HAXPES (Figure 4a), which is a direct consequence of the increased probing depth (in combination with a reduced cross-section for photoionization of the shallow C 1s core-level).  $\text{Li}_2\text{O}/\text{LiOH}$  surface species could still be detected (i.e., O 1s at  $530.2\pm 0.2\text{ eV}$ ), although their relative peak intensities were significantly reduced with respect to those from the LLZO lattice (i.e., O 1s at  $527.6\pm 0.2\text{ eV}$ , Li 1s at  $53.7\pm 0.2\text{ eV}$ , Zr 4s at  $50.6\pm 0.2\text{ eV}$ ). HAXPES analysis after successive sputtering steps is not able to remove the  $\text{Li}_2\text{O}/\text{LiOH}$  species fully, although the respective O 1s peak intensity decreases relatively to that of O in the LLZO lattice (Figure 4b,c).

This indicates that the  $\text{Li}_2\text{O}/\text{LiOH}$  species are not only present as a surface reaction layer, but are also formed along grain boundaries and open pores which intersect at the heat-treated

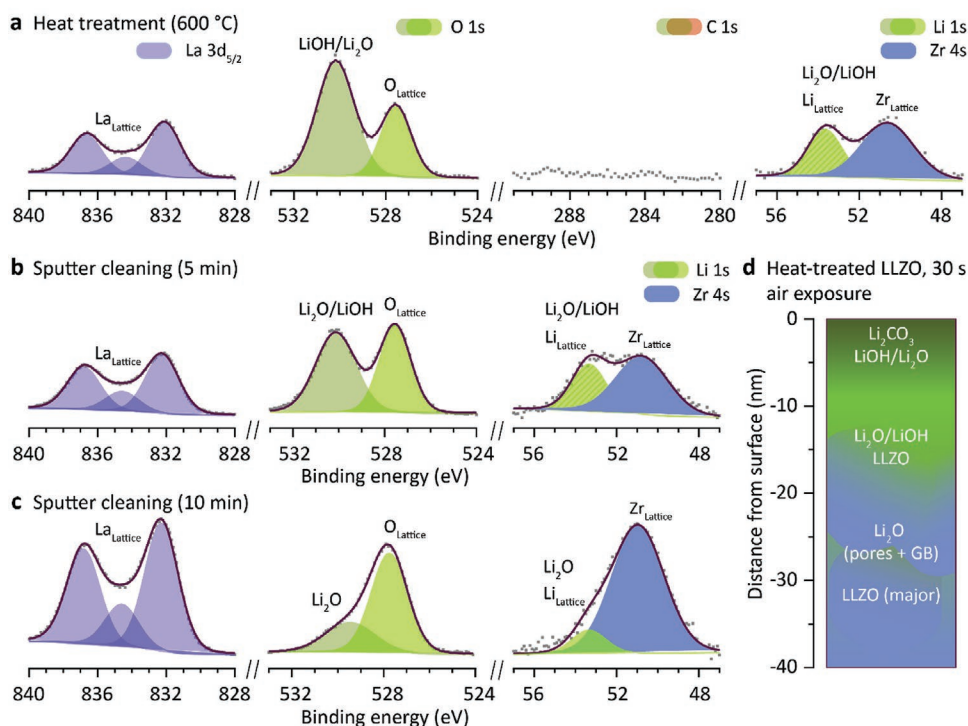


**Figure 4.** La 3d<sub>5/2</sub>, O 1s, C 1s, and Li 1s HAXPES spectra of a LLZO surface after a) heat-treatment (600 °C, 1 h, under Ar) and a brief exposure to air (<30 s), b) sputter cleaning for 5 min (depth of ≈10 nm), and c) sputter cleaning for 10 min (depth of ≈20 nm). d) Schematic composition of the heat-treated LLZO surface after minimal (<30 s) exposure to air. Note the presence of Li<sub>2</sub>O and LiOH within the pores and along grain boundaries (GB) that intersect with the outer surface.

LLZO surface (which is impossible to fully remove by gently sputter cleaning). In this regard, it is noted that the heat treatment at 600 °C mainly removes Li<sub>2</sub>CO<sub>3</sub> and LiOH species; Li<sub>2</sub>O cannot evaporate or decompose at this temperature. Short air exposure of the heat-treated LLZO probably introduces some hydroxylation of remaining Li<sub>2</sub>O species at the surface and along grain boundaries and pores. In conclusion, the combined XPS/HAXPES analysis gives some new insights about the depth-resolved surface composition of the heat-treated LLZO surface after short air exposure (<30 s), as illustrated in Figure 4d. The current XPS/HAXPES findings are commensurate with the surface contamination layer thickness value of < 10 nm obtained from soft X-ray absorption spectroscopy measurements, as reported by Cheng et al.<sup>[11]</sup> Gentle sputter cleaning can be used as an effective approach to remove Li-ion insulating Li<sub>2</sub>CO<sub>3</sub> and LiOH species from the outer LLZO surface.

The above XPS/HAXPES findings indicate that a relatively clean LLZO surface is established by the heat-treatment in a shielding atmosphere at 600 °C. As a next step, the heat-treated LLZO surface was coated with a thin Sb film with a nominal thickness of 50 nm (without intermediate exposure to air). The resulting Sb/LLZO system was investigated by lab-based HAXPES prior to sputtering, as well as after successive sputtering steps, in order to reveal the unperturbed chemical state of Sb at the buried Sb/LLZO interface (see Figure 5). The calculated probing depths for the La 3d, O 1s – Sb3d<sub>5/2</sub>, C 1s and Li 1s photoelectron lines, as recorded from the Sb/LLZO

system using Cr-Kα X-ray radiation equal 16.0, 16.8, 17.6, and 19.2 nm, respectively. These probing depths are much larger than the typical thickness of the mixing zone in Sb and LLZO as induced by sputtering with 1 kV Ar ions at an incident angle of 45° (i.e., up to about 5 nm, as estimated by Monte-Carlo simulations using the SRIM freeware). This implies that successive cycles of sputtering and HAXPES analysis allows probing the unperturbed chemical states at the buried Sb/LLZO interface, which is not possible by conventional XPS sputter-depth profiling (using a soft X-ray source). HAXPES analysis of the Sb/LLZO system before sputtering only probes the 50 nm Sb overlayer, since substrate signals from La or Zr are not detected (Figure 5, sputter time of 0 min). The Sb film is mainly composed of Sb and Sb<sub>2</sub>O<sub>3</sub>, as evidenced from the Sb 3d<sub>5/2</sub> peaks at 528.4 eV and 530.0 eV, respectively (as well as the intense plasmon peak from the Sb 4d photoelectron line at 48.4 eV,<sup>[27]</sup> which overlaps with the Zr 4s and Li 1s peaks). The La 3d<sub>5/2</sub> and Zr 3d<sub>5/2</sub> LLZO substrate intensities (i.e., La<sub>Lattice</sub> and Zr<sub>Lattice</sub>) are first detected after 10 mins of sputtering, while the unperturbed Sb/LLZO interface is most effectively probed by HAXPES for sputtering times between 20 and 30 mins. Notably, HAXPES analysis does not detect any Li<sub>2</sub>CO<sub>3</sub> and Li<sub>2</sub>O/LiOH species at the unperturbed Sb/LLZO interface (as is the case for the heat-treated LLZO surface without an Sb overlayer; see Figure 4b). This striking observation suggests that the deposition of Sb on the heat-treated LLZO surface can thermally activate a chemical reaction between Sb and remaining Li<sub>2</sub>O/LiOH species at the heat-treated LLZO surface to form LiSbO<sub>3</sub>.<sup>[28]</sup> Unfortunately,

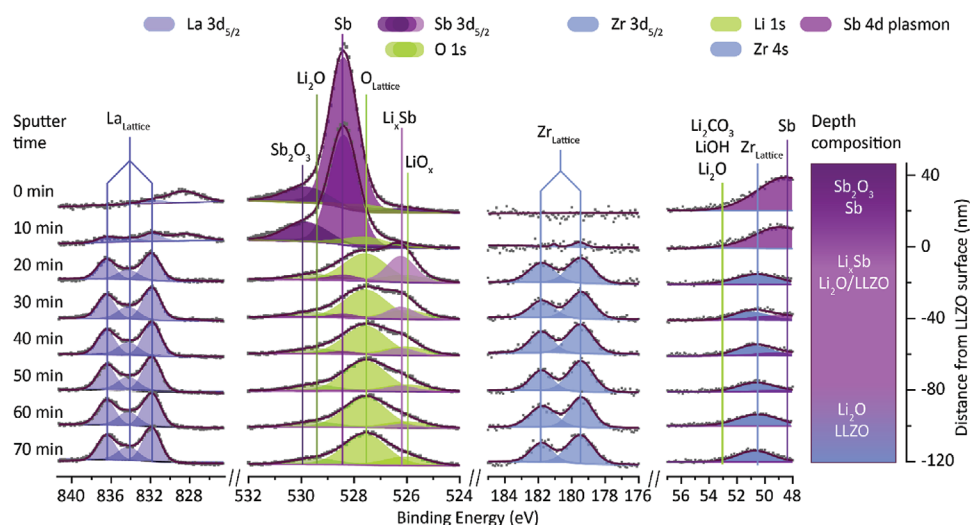


**Figure 5.** La  $3d_{5/2}$ , Sb  $3d_{5/2}$ , O 1s, Zr  $3d_{5/2}$ , Li 1s, Zr 4s, and Sb 4d HAXPES depth profile of a heat-treated LLZO surface, sputter-coated by  $\approx 50$  nm Sb layer.

the individual O 1s and  $3d_{5/2}$  spectral contributions from  $Sb_2O_3$  and  $LiSbO_3$  cannot be resolved, since the respective chemical shift is too small (i.e., of the order of the peak width). Interestingly, contrary to  $Li_2CO_3$  and  $LiOH$  compounds, which both possess a very low Li-ion conductivity of  $10^{-7}$  mS  $cm^{-1}$ ,<sup>[29]</sup> the literature suggests that  $LiSbO_3$  can be considered as a compelling Li-ion conductor, although no direct measurements of its Li-ion conductivity have been performed so far.

Even more striking than the absence of  $Li_2O/LiOH$  reaction products at the buried Sb/LLZO interface is the observation of an additional chemical species of Sb at  $526.2 \pm 0.2$  eV, which has a significantly lower BE than the metallic Sb  $3d_{5/2}$  peak at  $528.4 \pm 0.1$  eV. The corresponding (negative) shift between metallic Sb and this interface species is as large as  $-2.2 \pm 0.2$  eV. Such a chemical species at the lower BE side of the metallic Sb  $3d_{5/2}$  peak can only be rationalized by the formation of a  $Li_xSb$  alloy at the Sb/LLZO interface (note: ionic compounds of Sb, such as  $Sb_2O_3$  and  $LiSbO_3$  should appear at the higher BE side of the metallic Sb  $3d_{5/2}$  peak). It is well established that there are only two intermetallic bulk compounds in the Li-Sb system, namely  $Li_3Sb$  and  $Li_2Sb$ , which both have very narrow ranges of homogeneity; moreover, there is negligible solid solubility of Li in Sb, while there is some solubility of Sb in liquid Li, albeit very small ( $<0.01$  at.% Sb)<sup>[30]</sup> The enthalpy of formation of both intermetallic phases is highly exothermic and much larger for  $Li_3Sb$  (i.e.,  $-300$  kJ  $mol^{-1}$ ) as compared to  $Li_2Sb$  ( $-195$  kJ  $mol^{-1}$ ).<sup>[30]</sup> Importantly, as revealed by Huggins et al.<sup>[31]</sup> Li-Sb alloys possess a high Li-ion conductivity of  $0.15$  mS  $cm^{-1}$  (at  $360$  °C), resulting in a low Li/LLZO interfacial resistance.

Additionally, the observed results indicate that the magnetron sputter-coating procedure likely has a double action. First, the plasma acts as a sputter-cleaning agent, mimicking the effect of Ar sputter cleaning observed on Figures 3 and 4. Second, the deposited Sb creates a physical protective barrier by Sb, preventing recontamination upon exposure to air during the quick sample transfer.

To verify the formation of  $Li_3Sb$  and/or  $Li_2Sb$  upon reaction with liquid Li, a liquid drop of Li with a temperature of

about  $250$  °C was placed next to an as-prepared Sb/LLZO sample at room temperature under a shielding atmosphere, and both entities were put in contact side-by-side. Next, the unknown depth of the Li-Sb reaction zone below the solidified Li wetting layer with of skewed geometry (i.e., the Li wetting layer become thinner with increasing distance from the contact side) was allocated by successive cycles of sputtering (with  $1$  kV  $Ar^+/2 \times 2$  mm<sup>2</sup>), while monitoring the evolution of the Sb  $3d_{5/2}$  – O 1s spectral region by HAXPES. The Li-Sb reaction zone was revealed after a total sputter time of about 5–6 h, which roughly corresponds to a depth of 1–2  $\mu m$  below the solidified Li surface (see Figure 6). The formation of an intermetallic  $Li_xSb$  species by the reaction of the Sb overlayer with molten Li is evident across a sputter depth of a few hundreds of nanometers. In the Li-Sb reaction zone, a dominant Sb  $3d_{5/2}$  peak from  $Li_xSb$  is present at the lower BE side of the metallic Sb  $3d_{5/2}$  peak, as also observed at the buried Sb/LLZO interface in Figure 5. The absolute BE scale for the Sb/LLZO sample in Figure 5 might be shifted by band bending effects. However, the Sb  $3d_{5/2}$  chemical shift between metallic Sb and  $Li_3Sb$  and/or  $Li_2Sb$  should be independent of band bending (and charging effects). Surprisingly, the chemical shift between Sb and the intermetallic  $Li_xSb$  compound formed by the liquid drop experiment is only  $-1.4 \pm 0.2$  eV, which is smaller than the respective shift  $-2.2 \pm 0.2$  eV, as determined for the Sb intermetallic species at the buried Sb/LLZO interface (see Figure 5). In the liquid drop experiment, there is an excess reservoir of liquid Li. The finite solubility of Sb in liquid Li<sup>[30]</sup> then favors fast and continuous dissolution of Sb in the Li melt to form the most stable intermetallic phase,  $Li_3Sb$ . On the contrary, for the deposition of a Sb overlayer on LLZO, the formation of a  $Li_2Sb$  and/or  $Li_3Sb$  interlayer will be rate-limited by the dissolution and solid-state diffusion of Li from the LLZO lattice into the Sb overlayer. Moreover, the solubility of Li into Sb is negligible.<sup>[30]</sup> Consequently, only a very thin  $Li_2Sb$  reaction layer (instead of the Li-rich  $Li_3Sb$  phase) forms at the Sb/LLZO interface during the Sb deposition step. This could rationalize the difference in chemical shifts between the intermetallic  $Li_xSb$  compounds

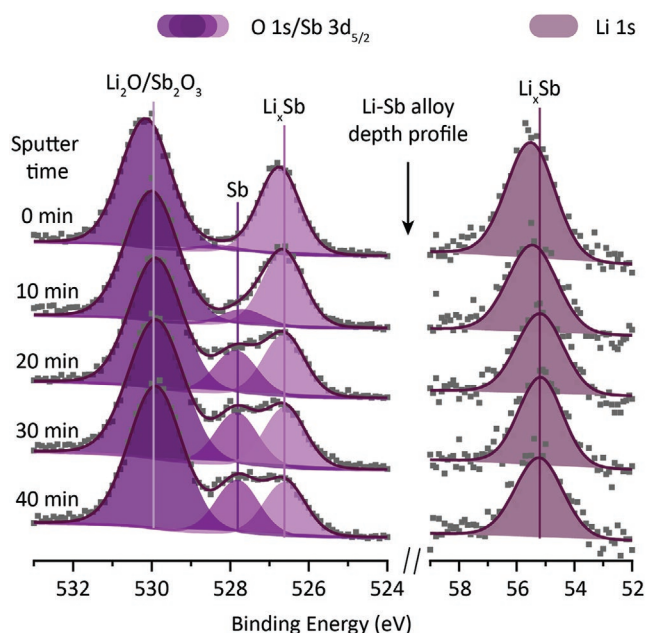


**Figure 6.** Sb  $3d_{5/2}$  and Li  $1s$  HAXPES sputter depth profile of a heat-treated LLZO pellet, sputter-coated by  $\approx 50$  nm layer of Sb, which was subsequently contacted with a liquid drop of Li (with a temperature of about  $250$  °C) under a shielding atmosphere. The sputter depth profile was recorded after removal of the solidified Li surface layer by gentle sputtering for 5–6 h using a  $1$  kV  $Ar^+$  beam (rastering an area of  $2 \times 2$  mm<sup>2</sup>), which roughly corresponds to a depth of  $1$ – $2$   $\mu$ m below the solidified Li surface.

formed in molten bulk Li (presumably  $Li_3Sb$ ) and at the buried Sb/LLZO interface (presumably  $Li_2Sb$ ). It could also explain why thicker Sb coatings of  $> 20$  nm were ineffective at reducing the interfacial resistance, since only the thin interfacial reaction layer of the Li-Sb alloy is Li-ion conductive.

Next, we 3D-mapped the elemental composition of the Li/Sb-coated LLZO interface (see **Figure 7a** for an SEM cross-section) using fluorine gas-assisted focused ion beam time-of-flight secondary ion mass spectroscopy (FIB-TOF-SIMS) (**Figure 7b**). This novel technique [32,33] combines an HV-compatible high-resolution TOF detector (HTOF) and an in situ gas injection system (GIS) within FIB/SEM (focused ion beam/scanning electron microscope) analytical chamber. The measured sample was composed of  $2$   $\mu$ m and  $200$  nm layers of Li and Cu, which were thermally evaporated on a  $10$ -nm-Sb-sputter-coated-LLZO pellet. Additionally, the sample was subjected to a brief heat-treatment at  $220$  °C ( $30$  min) to ensure an efficient Li-Sb alloy formation, copying the preparation procedure for electrochemical measurements. We emphasize that the detection of such small amounts of Sb under standard vacuum conditions (positive ion detection mode, without  $XeF_2$  co-injection) is challenging due to low ionization efficiency of this element. However, the introduction of fluorine has increased the yield of positive ions considerably. As follows from **Figure 7b**, the Sb ion signal was measured across the entire sample with the highest signal intensity at the Li/LLZO interface, pointing to the fact that the migration of Sb occurs into both the Li and LLZO. SEM images of the topology acquired before and after FIB-TOF-SIMS measurements, as well as 2D chemical maps and

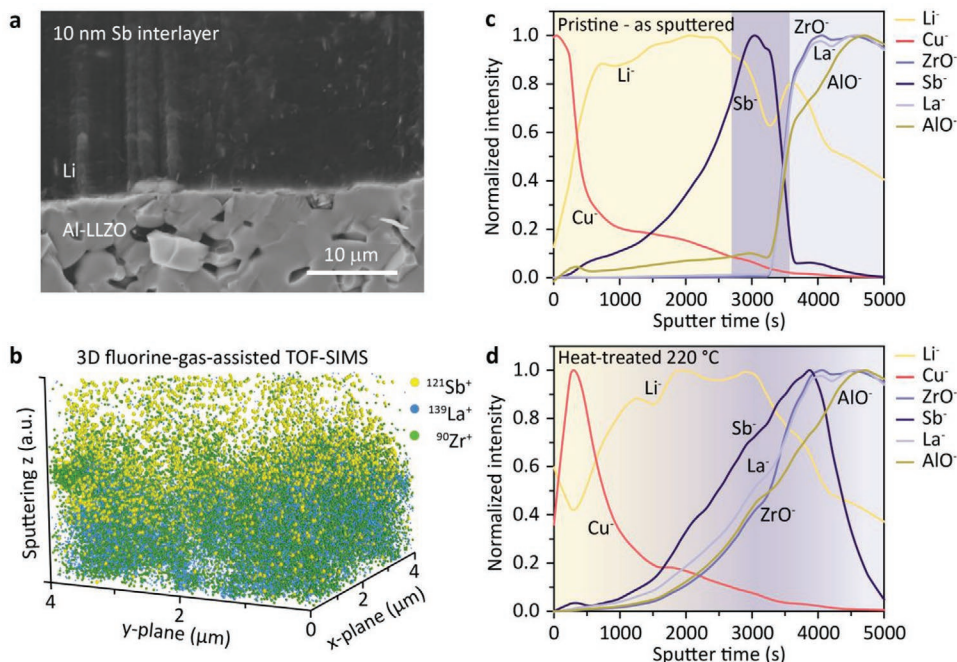


**Figure 7.** a) Cross-section SEM image of the interface between LLZO pellet and Li. b) 3D elemental structure of the Sb-containing interface between Li and LLZO pellet measured by FIB-TOF-SIMS. c) Cryo TOF SIMS depth profile of a pristine Li/Sb-coated LLZO interface. d) Cryo TOF-SIMS depth profile of the Li/Sb-coated LLZO interface after a heat treatment at  $220$  °C.

TOF-SIMS depth profiles can be found in the Figures S4–S6 in the Supporting Information.

Moreover, aiming to exclude an impact of the low melting temperature of Li on the distribution of the detected species across the interface, additional TOF-SIMS depth-profile measurements were performed at cryogenic temperature, before and after a heat treatment at 220 °C (Figure 7c,d). The obtained results also confirmed the blurriness of the Cu/Li/Sb-coated LLZO interfaces with a wide distribution of Sb, Li, La, Zr and Al species across the interface region. They also demonstrate the mobility of the Sb species at the interface, indicating that the Sb at the interface is likely to migrate and dilute during the battery operations as well.

Another possible reaction of the Sb with other elements is not to be excluded. Yang et al.<sup>[34]</sup> reported Sb doping of Al-LLZO. They show that Sb is partly replacing the Zr and Li in the octahedral and the 24d tetrahedral sites of Al-LLZO structure, respectively. The estimated Li-ion conductivity of Sb-doped Al-LLZO ceramics was  $\approx 0.41 \text{ mS cm}^{-1}$  at RT. In this context, one can speculate that Sb acting as a dopant can provide a highly conductive layer at the surface of the LLZO pellet.

### 2.3. Electrochemical Measurements

To examine the impact of the Sb coating on the effectiveness of the Li plating/stripping at the LLZO/Li interface, symmetrical cells were prepared by isostatically pressing Li on Sb-coated or only heat-treated LLZO pellets, followed by their heating at 220 °C under inert atmosphere. In accordance with Ohm's law

and the impedance measurements, the overpotential of the symmetrical cells comprising Sb-coated LLZO pellets is increasing at the increase of Sb-coating thickness from 10 to 100 nm (see Figure S7 in the Supporting Information). Then, galvanostatic cycling experiments were conducted at room temperature using current densities of 0.05 and 0.1  $\text{mA cm}^{-2}$  (first 2 cycles) and then 0.2  $\text{mA cm}^{-2}$  with a capacity limitation of 0.1  $\text{mAh cm}^{-2}$  per half-cycle without the employment of external pressure.

The galvanostatic voltage profiles of symmetrical cells are shown in Figure 8a. As anticipated from the impedance spectroscopy measurements (Figure 2; Figure S2, Supporting Information), the heat-treated and the Sb-coated samples display very similar overpotentials in the early stages of galvanostatic cycling. However, after 50 cycles (cumulative capacity of 10  $\text{mAh cm}^{-2}$ ), the overpotential of the heat-treated sample starts to increase significantly. Cycling of the heat-treated system can be extended for weeks without short-circuit, but with large overpotential values of 1 V and  $-1 \text{ V}$  for each half-cycle. These data are in line with cross-section SEM images (Figure 8b) taken before and after cycling, which indicate the formation of huge voids and Li whiskers at the Li/LLZO interface without Sb coating. The latter leads to a reduction of Li/LLZO contact area, which translates into a higher interfacial resistance and steep voltage curves during the stripping of Li. On the contrary, the Sb-coated system can be cycled up to 70  $\text{mAh cm}^{-2}$  of cumulative capacity with only a minor increase of the overpotential up to 40–45 mV. The cross-sectional SEM images (Figure 8c) of Li/Sb-coated-LLZO interface before and after cycling clearly display the superior adhesion of Li on Sb-coated LLZO.

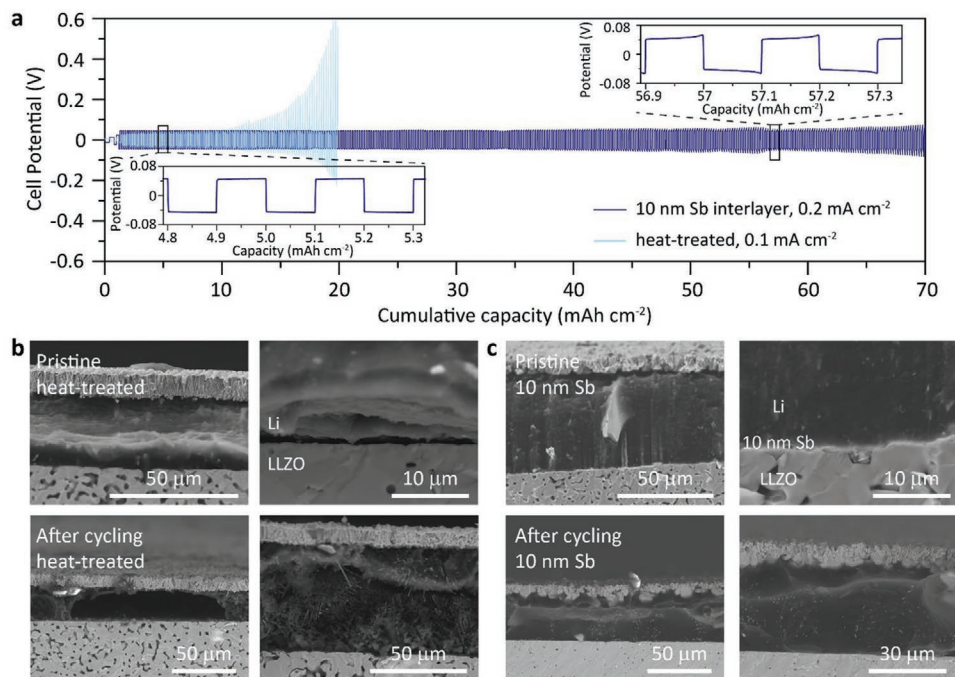


**Figure 8.** a) Voltage profiles of Li/LLZO/Li symmetrical cells comprising Sb-coated and uncoated LLZO pellets at current densities of 0.05 and 0.1  $\text{mA cm}^{-2}$  (first 2 cycles) and 0.2  $\text{mA cm}^{-2}$  (from 3<sup>rd</sup> cycle onward). The measurements were performed at room temperature, without the employment of external pressure, and with a capacity limitation of 0.1  $\text{mAh cm}^{-2}$  per half-cycle. b) Cross-section SEM images of a pristine and cycled symmetrical cell composed of a heat-treated LLZO pellet without Sb coating. c) Cross-section SEM micrographs of a pristine and cycled sample symmetrical cell comprising Sb-coated LLZO pellet.

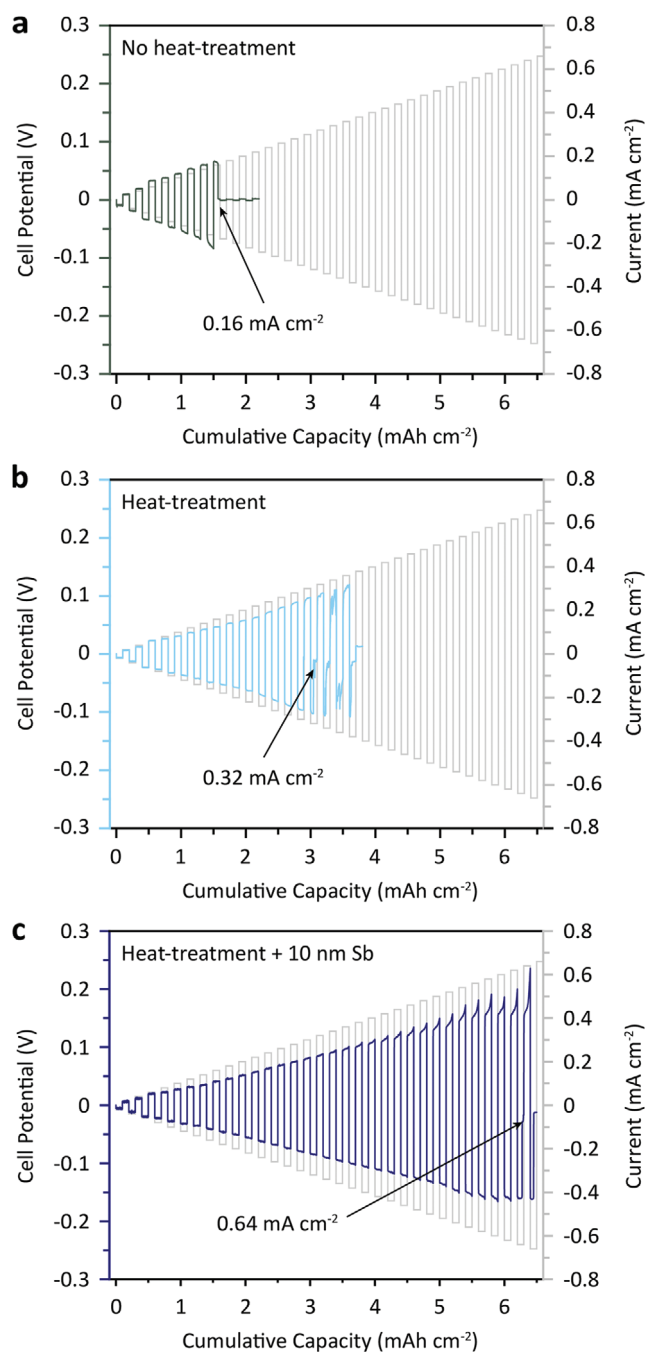


**Figure 9.** a) Comparison of voltage profiles of Li/LLZO/Li symmetrical cells comprising non-heat treated, b) heat-treated (600 °C, 1 h), and c) Sb-sputtered-heat-treated LLZO pellet, measured at different current densities. The measurements were conducted at room temperature, without employment of external pressure and with capacity limitation of 0.1 mAh cm<sup>-2</sup> per half-cycle.

To assess the achievable critical current density (CCD) of the studied systems, which is the current density at which the propagation of the Li dendrites/filaments starts, galvanostatic cycling experiments were performed by increasing the current density in steps of 0.02 mA cm<sup>-2</sup>, and transferring the same

amount of Li for each half cycle (0.1 mAh cm<sup>-2</sup>). The tests were conducted at room temperature without applying any stack pressure. **Figure 9** depicts a comparison of three symmetrical cells composed of non-heat-treated, heat-treated, and Sb-coated LLZO pellets. Both non-heat-treated and heat-treated LLZO pellets demonstrate relatively low CCDs of 0.16 and 0.32 mA cm<sup>-2</sup>, pointing to the fact that the presence of LiOH and Li<sub>2</sub>CO<sub>3</sub> significantly hinders plating/stripping of Li. Those results are in line with published values for a heat-treated surface.<sup>[14]</sup> On the contrary, a much higher CCD of 0.64 mA cm<sup>-2</sup> was reproducibly reached for a symmetrical cell with a Sb-coated pellet.

With regular LLZO samples, voids form because the diffusion of Li into the LLZO is faster than the ad-atom diffusion of Li in the Li metal.<sup>[35]</sup> The Li vacancies are not replenished fast enough, and therefore interface voids appear. This effect is accentuated by the presence of patches of Li-ion insulating Li<sub>2</sub>CO<sub>3</sub> and LiOH on the surface, which leads to current focusing and faster void formation. To understand the CCD enhancement, it is helpful to compare the Li diffusion coefficients of the materials involved in the studied system, namely Li, Li<sub>3</sub>Sb and LLZO. The self-diffusion coefficient in solid Li at 25 °C is 765 × 10<sup>-11</sup> cm<sup>2</sup> s<sup>-1</sup>.<sup>[36]</sup> This value is much lower than the Li diffusion in Li<sub>3</sub>Sb with 3.5 × 10<sup>-9</sup> cm<sup>2</sup> s<sup>-1</sup><sup>[37]</sup> and LLZO with ≈ 2 × 10<sup>-9</sup>–8 × 10<sup>-9</sup> cm<sup>2</sup> s<sup>-1</sup><sup>[38]</sup> (both at 25 °C). According to Krauskopf et al,<sup>[35]</sup> from a physical and chemical point of view, the alloying interlayer fulfils two main functions. Firstly, it acts as a mediator during the cell assembly providing a good and homogeneous contact. This enhanced contact will homogeneously distribute the current density over the whole surface, preventing current focusing effects. The latter usually arises from the presence of insulating islands at the surface of LLZO. In our experiments, the sputter-coating process was additionally homogenizing the surface by cleaning it and physically preventing its recontamination. Secondly, it regulates the diffusion kinetics at Li/Li<sub>3</sub>Sb and Li<sub>3</sub>Sb/LLZO interfaces. A Li-Sb alloy layer with Li diffusion faster than in pure Li will lead to faster Li transport toward the Li/Li<sub>3</sub>Sb interface. At the Li<sub>3</sub>Sb/LLZO interface, however, the diffusion coefficient of LLZO is only slightly higher. Should the alloy layer have a lower diffusivity, still no pores will form at the interface. The Li concentration will rather decrease in the interlayer region close the Li<sub>3</sub>Sb/LLZO interface, causing a slight increase in overpotential. However, the contact loss of the electrodes will be prevented, which means that no current focusing will take place during the subsequent plating/stripping. In the present system, the Li-Sb alloy imparts an enhanced Li-transfer kinetics at the interface, as evident from electrochemical impedance spectroscopy measurements (Figure 2).

Next, we probed electrochemical functionality of the developed Sb based Li/LLZO interface in full hybrid-type cells. It should be noted that the development of LLZO based all-solid-state cathodes is still at its infancy stage. This is due to a poor LLZO/cathode contact, caused on the one hand by the necessity of high-temperature co-sintering (leading to the formation of insulating interfaces) and on the other hand by volume changes of cathode active material upon cycling.<sup>[2]</sup> Consequently, in this work, for assembly of the full cell, we used a so-called paste cathode, where the active material is mixed with carbon black and ionic liquid (IL), providing sufficient levels of electronic

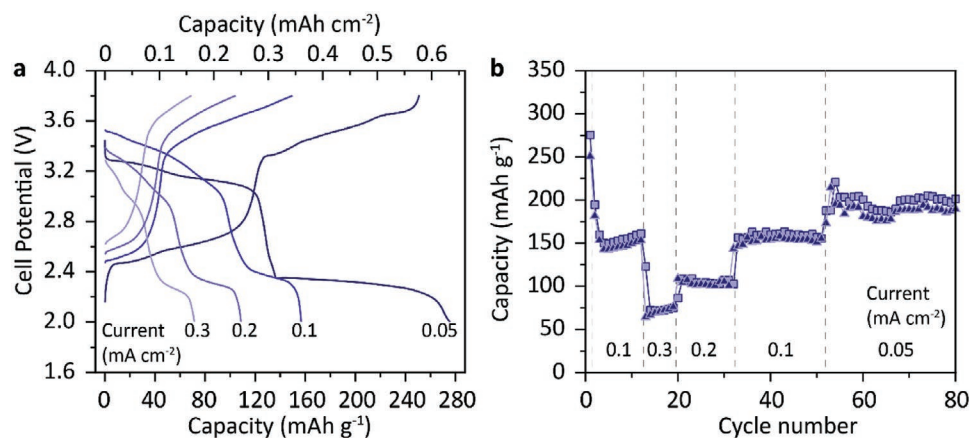


**Figure 10.** a) Typical galvanostatic charge-discharge voltage profiles and b) cyclic stability measurements of  $V_2O_5|Sb$ -coated-LLZO|Li full cell at current densities of 0.05, 0.1, 0.2, and 0.3  $mA\ cm^{-2}$ .

and ionic conductivity, accordingly.<sup>[19]</sup> Ionic liquids have indeed been proven to significantly improve the ionic transport at the cathode/LLZO interface, as reported by Passerini et al.<sup>[39]</sup> As a cathode material, we chose vanadium pentoxide ( $V_2O_5$ )<sup>[40]</sup> because of its high theoretical capacity upon lithiation (274  $mAh\ g^{-1}$  for the two-electron reaction) and relatively high average discharge voltage of 2.6 V versus  $Li^+/Li$ . This indicates that in combination with a metallic lithium anode, it may offer an energy density of up to 712  $Wh\ kg^{-1}$ . This is higher than that of  $LiFePO_4$  (578  $Wh\ kg^{-1}$ ),  $LiNi_{1/3}Mn_{1/3}Co_{1/3}O_2$  (610  $Wh\ kg^{-1}$ ) and  $LiCoO_2$  (546  $Wh\ kg^{-1}$ ) commercial Li-ion cathodes. Moreover, to the best of our knowledge, a  $V_2O_5$  cathode has not been investigated in Li-garnet SSBs.

In short, the paste was prepared by mixing 240 mg of  $V_2O_5$  (41 wt.%), 80 mg of CB (13.7 wt.%) and 119  $\mu l$  of 0.3M LiTFSI in  $PY_{14}$ TFSI ionic liquid electrolyte (45.3 wt.%). The paste electrode was deposited directly on the heat-treated surface of LLZO, and then covered with an Al foil current collector. The average loading of  $V_2O_5$  active material was  $\approx 2.3\ mg\ cm^{-2}$ . The cells were tested at room temperature and without applying external pressure. The applied currents were normalized to the surface area of the Li anode.

**Figure 10a** shows the voltage profiles of a  $V_2O_5|Sb$ -coated-LLZO|Li full cell measured at different current densities of 0.05, 0.1, 0.2, and 0.3  $mA\ cm^{-2}$ . During a discharge step, i.e., a lithiation of the cathode, three distinct plateaus at approximately 3.3, 3.1 and 2.3 V versus  $Li^+/Li$  were observed at all current densities, indicating a 3-step lithiation mechanism. As previously reported,<sup>[41]</sup> the first and second plateaus are attributed to the formation of  $Li_{0.5}V_2O_5$  and  $LiV_2O_5$ , respectively. The third plateau corresponds to the phase transition from  $LiV_2O_5$  to  $Li_2V_2O_5$ . The results demonstrate that the increase of the current density from 0.05, 0.1  $mA\ cm^{-2}$ , and then to 0.3  $mA\ cm^{-2}$  leads to significant decrease of reversible charge storage capacity from 250  $mAh\ g^{-1}$  (0.58  $mAh\ cm^{-2}$ ) to 157  $mAh\ g^{-1}$  (0.35  $mAh\ cm^{-2}$ ) and 71  $mAh\ g^{-1}$  (0.16  $mAh\ cm^{-2}$ ), respectively. However, when the current density was decreased back to 0.2  $mA\ cm^{-2}$ , 0.1  $mA\ cm^{-2}$  and 0.05  $mA\ cm^{-2}$ , nearly complete capacity recovery with 109, 157 and  $\approx 200\ mAh\ g^{-1}$  (0.45  $mAh\ cm^{-2}$ ) was achieved (**Figure 10b**). A significant drop in capacity at high current density underlines the necessity for improving

the charge-transfer properties of the  $V_2O_5$  cathode/LLZO interface and Li-ion/electronic percolation within the composite  $V_2O_5$  cathode. Similar full-cell measurements with a  $LiNi_{0.5}Mn_{0.3}Co_{0.2}O_2$  paste cathode were performed with the same composition. They can be found in the Supporting information (Figure S8, Supporting Information).

### 3. Conclusion

We have examined Sb as a compelling interfacial layer between LLZO solid-state electrolyte and metallic Li, enabling to improve the Li wettability on the LLZO surface. A side-by-side comparison of Sb layers of different thicknesses on the order of 5 to 100 nm showed that the areal specific interface resistance of a LLZO pellet sputtered with  $\approx 10$  nm Sb layer has the lowest value of 4.1(1)  $\Omega\ cm^2$  compared to those of thinner (5 nm), thicker (20–100 nm) Sb coatings or non-coated LLZO surface. We determined that the Li/10-nm-Sb-LLZO/Li symmetrical cells exhibit a high critical current density of up to 0.64  $mA\ cm^{-2}$  and low overpotentials of 40–50 mV at a current density of 0.2  $mA\ cm^{-2}$  at room temperature and without the employment of external pressure. Using an advanced set of surface characterization methods such as XPS/HAXPES and TOF-SIMS, we revealed that the major factor governing an efficient plating/stripping of Li at the Sb-coated LLZO surface is the formation of a Li-Sb alloy, which enables an efficient Li-ion and electronic percolation at the Li/LLZO interface and effectively mitigates the formation of cavities and Li whiskers upon plating/stripping of Li. The electrochemical performance of Sb-coated LLZO solid-state electrolyte has also been assessed with an intercalation-type  $V_2O_5$  cathode. Li/Sb-coated-LLZO/ $V_2O_5$  full cells delivered stable areal capacities of around 0.45  $mAh\ cm^{-2}$ , with a peak current density of 0.3  $mA\ cm^{-2}$ .

### 4. Experimental Section

**Preparation of Garnet Al-LLZO Pellets:** Commercial LLZO powder (Ampcera™, Al-doped LLZO, 500 nm nano-powder) was pressed uniaxially inside of 10 or 13  $mm^2$  pressing dyes at the pressure of  $\approx 15$  kN. The obtained green pellets were further isostatically pressed at 1000 kN

and subsequently pre-polished from all sides with polishing paper to remove any impurities at the surface. Then, polished green pellets were covered from every side with pristine LLZO powder and sandwiched between two Al<sub>2</sub>O<sub>3</sub> crucible lids prior to their insertion into a tube furnace (Gero Carbolite). The sintering of the pellets was performed at 1220 °C for 15 min (heating rate to 1220 °C: 450 °C h<sup>-1</sup>, cooling rate to 700 °C: 240 °C h<sup>-1</sup>, followed by natural cooling) under a nitrogen atmosphere with constant gas flow. Afterward, the sintered pellets were coarse-polished down to a thickness of 1 mm, followed by fine polishing with a grit size of 1200. The resulting pellets were then placed on ≈5 mm thick LLZO pillars and heat-treated in an Ar glovebox at 600 °C for 1 h.

**Characterization:** **Powder X-ray diffraction (XRD)** was measured on a STOE STADI P powder X-ray diffractometer in reflection mode (Mo-Kα1 irradiation, λ = 0.7093 Å). SEM and **EDX analysis** was performed using a Hitachi TM3030Plus Tabletop microscope with an acceleration voltage of 10 kV. **XPS/HAXPES** analysis was performed using a PHI Quantes spectrometer (ULVAC-PHI), equipped with a conventional low-energy Al-Kα source (1486.6 eV) and a high energy Cr-Kα (5414.7 eV) X-ray source. Both sources are high flux focused monochromatic X-ray beams. The energy scale of the hemispherical analyzer was calibrated according to ISO 15 472 by referencing the Au 4f<sub>7/2</sub> and Cu 2p<sub>3/2</sub> main peaks (as measured in situ for corresponding sputter-cleaned, high-purity metal references) to the recommended BE positions of 83.96 eV and 932.62 eV, respectively. Charge neutralization during each measurement cycle was accomplished by a dual beam charge neutralization system, employing low energy electron and argon ion beams (1 V Bias, 20 μA current). More details can be found in the Supporting Information. **TOF-SIMS** depth profiling was performed with an UHV dedicated standalone TOF-SIMS<sup>5</sup> system from IONTOF (Germany). For sputtering, a Cs<sup>+</sup>-ion gun was employed with an acceleration voltage of 2 kV on an area of 300 × 300 μm<sup>2</sup>. The primary ion source used for analyzing was Bi<sup>+</sup> ions with an acceleration voltage of 25 kV. The negative-charged ions extracted from a 50 × 50 μm<sup>2</sup> area within the sputtering crater were used for the analysis. The measurements were performed in the negative mode without a GIS system. For the **fluorine gas-assisted 3D FIB-TOF-SIMS measurements**, a novel approach<sup>[32,42]</sup> of combining a HV-compatible high-resolution TOF-SIMS detector (HTOF from TOFWERK, Switzerland) with an in-situ gas injection system integrated within a FIB-SEM (Tescan, Czech Republic) was used. The sample was bombarded with a 20 kV <sup>69</sup>Ga<sup>+</sup> primary ion beam (used for sputtering and analysis), and the 4D data set (x,y,z and associated mass spectrum for each data point) was obtained at approx. 114 ± 1 pA ion current and 32 μs dwell time from a 10 μm × 10 μm area with 512 × 512 pixels and 2 × 2 binning. The depth profiles of positive ions were acquired from the central 5 μm × 5 μm area to prevent potential edge effect artifacts. Mass spectra were calibrated using the secondary ion signals of the main sample elements (<sup>7</sup>Li<sup>+</sup>, <sup>27</sup>Al<sup>+</sup>, <sup>63</sup>Cu<sup>+</sup>, <sup>121</sup>Sb<sup>+</sup> and <sup>139</sup>La<sup>+</sup>) and the primary ion beam (<sup>69</sup>Ga<sup>+</sup>). More details can be found in the Supporting Information.

**Sb Coating:** Sb was sputtered at room temperature onto the LLZO pellets by a radio frequency magnetron sputtering (Orion, AJA International Inc.). The films were prepared using an Sb target (Plasmaterials) under Ar flow (50 sccm). The film thickness was tuned by measuring the deposition rate with a quartz crystal microbalance (QCM) and adjusting the deposition time accordingly.

**Symmetrical Cell Preparation:** Symmetrical cells comprising non-heat-treated, heat-treated and Sb-coated Al-LLZO pellets were prepared using an identical procedure: 6 or 8 mm wide discs of laminated Li (50 μm) on Cu foil (9 μm) were isostatically pressed at 1000 kN for at least 10 min onto the opposite sides of Al-LLZO pellet under inert conditions. Then, the resulting symmetrical cells were heat-treated at 220 °C on a heating plate under an inert Ar atmosphere (30 min for each side).

**The Preparation of the V<sub>2</sub>O<sub>5</sub> Cathode Paste:** V<sub>2</sub>O<sub>5</sub> cathode paste was prepared by mixing powders of vanadium pentoxide (240 mg, GfE) and carbon black Super P (80 mg, Imerys) with 0.3M LiTFSI (99%, Sigma Aldrich) in PY14TFSI (99%, Sigma Aldrich) ionic liquid (190 μl), corresponding to a V<sub>2</sub>O<sub>5</sub> weight content of ≈41 wt%. The mixture was ground thoroughly for at least 15 min in a mortar under inert conditions, followed by its casting onto a bare surface of heat-treated Al-LLZO using

a spatula. Afterwards, the prepared electrode was covered with an Al foil current collector.

**Electrochemical Testing:** Symmetrical and full cells were tested inside of the Ag glovebox using a multichannel workstation (MPG-2, Bio-Logic SAS). Cells were placed between two coin-cell spacers and fixed by clamps with negligible pressure of 0.15 MPa. Electrochemical impedance spectroscopy measurements were conducted using a frequency range of 10 MHz to 0.1 Hz with a sinus amplitude of 10 mV. Symmetrical cells were cycled in galvanostatic mode using current densities of 0.02–1.2 mA cm<sup>-2</sup>, transferring typically 0.1 mAh cm<sup>-2</sup> per semi cycle. Full cell testing was performed in a voltage range from 3.8 to 2.0 V, with current densities from 0.05 to 0.3 mA cm<sup>-2</sup>. Typical active material loadings was ≈2.3 mg cm<sup>-2</sup>.

## Supporting Information

Supporting Information is available from the Wiley Online Library or from the author.

## Acknowledgements

K.V.K. and M.V.K. acknowledge partial financial support from Empa-Fraunhofer ICS project “IE4B” (under ICON funding scheme). The authors are grateful to the research facilities of ETH Zurich (ETH Electron Microscopy Center, Department of Chemistry and Applied Biosciences) and Empa (Empa Electron Microscopy Center and Laboratory for Mechanics of Materials & Nanostructures) for access to the instruments and for technical assistance.

## Conflict of Interest

The authors declare no conflict of interest.

## Data Availability Statement

The data that support the findings of this study are available from the corresponding author upon reasonable request.

## Keywords

antimony, critical current density, interfacial layers, Li-ion batteries, LLZO, solid-state batteries, symmetrical cells

Received: July 9, 2021

Revised: August 6, 2021

Published online:

- [1] a) X.-B. Cheng, R. Zhang, C.-Z. Zhao, Q. Zhang, *Chem. Rev.* **2017**, *117*, 10403; b) J. Janek, W. G. Zeier, *Nat. Energy* **2016**, *1*, 16141; c) D. Lin, Y. Liu, Y. Cui, *Nat. Nanotechnol.* **2017**, *12*, 194; d) S. Randau, D. A. Weber, O. Kötz, R. Koerver, P. Braun, A. Weber, E. Ivers-Tiffée, T. Adermann, J. Kulisch, W. G. Zeier, F. H. Richter, J. Janek, *Nat. Energy* **2020**, *5*, 259.
- [2] K. J. Kim, M. Balaish, M. Wadaguchi, L. Kong, J. L. M. Rupp, *Adv. Energy Mater.* **2021**, *11*, 2002689.
- [3] a) A. J. Samson, K. Hofstetter, S. Bag, V. Thangadurai, *Energy Environ. Sci.* **2019**, *12*, 2957; b) K. V. Kravchik, F. Okur, M. V. Kovalenko, *ACS Energy Lett.* **2021**, *6*, 2202.

- [4] C. Wang, K. Fu, S. P. Kammampata, D. W. McOwen, A. J. Samson, L. Zhang, G. T. Hitz, A. M. Nolan, E. D. Wachsman, Y. Mo, V. Thangadurai, L. Hu, *Chem. Rev.* **2020**, *120*, 4257.
- [5] S. Afyon, K. V. Kravchuk, S. Wang, J. v. d. Broek, C. Hänsel, M. V. Kovalenko, J. L. M. Rupp, *J. Mater. Chem. A* **2019**, *7*, 21299.
- [6] a) Q. Liu, Z. Geng, C. Han, Y. Fu, S. Li, Y.-b. He, F. Kang, B. Li, *J. Power Sources* **2018**, *389*, 120; b) K. Kerman, A. Luntz, V. Viswanathan, Y.-M. Chiang, Z. Chen, *J. Electrochem. Soc.* **2017**, *164*, A1731.
- [7] X. Han, Y. Gong, K. Fu, X. He, G. T. Hitz, J. Dai, A. Pearse, B. Liu, H. Wang, G. Rubloff, Y. Mo, V. Thangadurai, E. D. Wachsman, L. Hu, *Nat. Mater.* **2017**, *16*, 572.
- [8] H. Huo, J. Luo, V. Thangadurai, X. Guo, C.-W. Nan, X. Sun, *ACS Energy Lett.* **2020**, *5*, 252.
- [9] W. Xia, B. Xu, H. Duan, X. Tang, Y. Guo, H. Kang, H. Li, H. Liu, *J. Am. Ceram. Soc.* **2017**, *100*, 2832.
- [10] A. Sharafi, S. Yu, M. Naguib, M. Lee, C. Ma, H. M. Meyer, J. Nanda, M. Chi, D. J. Siegel, J. Sakamoto, *J. Mater. Chem. A* **2017**, *5*, 13475.
- [11] L. Cheng, E. J. Crumlin, W. Chen, R. Qiao, H. Hou, S. F. Lux, V. Zorba, R. Russo, R. Kostecki, Z. Liu, K. Persson, W. Yang, J. Cabana, T. Richardson, G. Chen, M. Doeff, *Phys. Chem. Chem. Phys.* **2014**, *16*, 18294.
- [12] L. Cheng, C. H. Wu, A. Jarry, W. Chen, Y. Ye, J. Zhu, R. Kostecki, K. Persson, J. Guo, M. Salmeron, G. Chen, M. Doeff, *ACS Appl. Mater. Interfaces* **2015**, *7*, 17649.
- [13] M. Wang, J. Sakamoto, *J. Power Sources* **2018**, *377*, 7.
- [14] A. Sharafi, E. Kazyak, A. L. Davis, S. Yu, T. Thompson, D. J. Siegel, N. P. Dasgupta, J. Sakamoto, *Chem. Mater.* **2017**, *29*, 7961.
- [15] H. Huo, Y. Chen, N. Zhao, X. Lin, J. Luo, X. Yang, Y. Liu, X. Guo, X. Sun, *Nano Energy* **2019**, *61*, 119.
- [16] M. M. Besli, C. Usubelli, M. Metzger, V. Pande, K. Harry, D. Nordlund, S. Sainio, J. Christensen, M. M. Doeff, S. Kuppen, *ACS Appl. Mater. Interfaces* **2020**, *12*, 20605.
- [17] N. J. Taylor, S. Stangeland-Molo, C. G. Haslam, A. Sharafi, T. Thompson, M. Wang, R. Garcia-Mendez, J. Sakamoto, *J. Power Sources* **2018**, *396*, 314.
- [18] K. Liu, R. Zhang, M. Wu, H. Jiang, T. Zhao, *J. Power Sources* **2019**, *433*, 226691.
- [19] Y. Shao, H. Wang, Z. Gong, D. Wang, B. Zheng, J. Zhu, Y. Lu, Y.-S. Hu, X. Guo, H. Li, X. Huang, Y. Yang, C.-W. Nan, L. Chen, *ACS Energy Lett.* **2018**, *3*, 1212.
- [20] K. Fu, Y. Gong, Z. Fu, H. Xie, Y. Yao, B. Liu, M. Carter, E. Wachsman, L. Hu, *Angew. Chem., Int. Ed.* **2017**, *56*, 14942.
- [21] W. Luo, Y. Gong, Y. Zhu, Y. Li, Y. Yao, Y. Zhang, K. Fu, G. Pastel, C.-F. Lin, Y. Mo, E. D. Wachsman, L. Hu, *Adv. Mater.* **2017**, *29*, 1606042.
- [22] W. Luo, Y. Gong, Y. Zhu, K. K. Fu, J. Dai, S. D. Lacey, C. Wang, B. Liu, X. Han, Y. Mo, E. D. Wachsman, L. Hu, *J. Am. Chem. Soc.* **2016**, *138*, 12258.
- [23] M. He, Z. Cui, C. Chen, Y. Li, X. Guo, *J. Mater. Chem. A* **2018**, *6*, 11463.
- [24] A. Junji, T. Akira, K. Kunimitsu, K. Norihito, I. Yasushi, A. Junji, *Chem. Lett.* **2011**, *40*, 60.
- [25] Y. Chen, E. Rangasamy, C. Liang, K. An, *Chem. Mater.* **2015**, *27*, 5491.
- [26] K. P. C. Yao, D. G. Kwabi, R. A. Quinlan, A. N. Mansour, A. Grimaud, Y.-L. Lee, Y.-C. Lu, Y. Shao-Horn, *J. Electrochem. Soc.* **2013**, *160*, A824.
- [27] W. K. Liu, W. T. Yuen, R. A. Stradling, *J. Vac. Sci. Technol., B: Nanotechnol. Microelectron.: Mater., Process., Meas., Phenom.* **1995**, *13*, 1539.
- [28] Y. Inaguma, A. Aimi, D. Mori, T. Katsumata, M. Ohtake, M. Nakayama, M. Yonemura, *Inorg. Chem.* **2018**, *57*, 15462.
- [29] a) S. Shi, Y. Qi, H. Li, L. G. Hector, *J. Phys. Chem. C* **2013**, *117*, 8579; b) R. T. Johnson, R. M. Biefeld, J. D. Keck, *Mater. Res. Bull.* **1977**, *12*, 577.
- [30] J. Sangster, A. D. Pelton, *J. Phase Equilibria* **1993**, *14*, 514.
- [31] W. Weppner, R. A. Huggins, *J. Solid State Chem.* **1977**, *22*, 297.
- [32] a) A. Priebe, I. Utke, L. Pethö, J. Michler, *Anal. Chem.* **2019**, *91*, 11712; b) A. Priebe, E. Huszar, M. Nowicki, L. Pethö, J. Michler, *Anal. Chem.* **2021**, *93*, 10261.
- [33] a) A. Priebe, L. Pethö, J. Michler, *Anal. Chem.* **2020**, *92*, 2121; b) A. Priebe, T. Xie, L. Pethö, J. Michler, *J. Anal. At. Spectrom.* **2020**, *35*, 2997.
- [34] T. Yang, Y. Li, W. Wu, Z. Cao, W. He, Y. Gao, J. Liu, G. Li, *Ceram. Int.* **2018**, *44*, 1538.
- [35] T. Krauskopf, F. H. Richter, W. G. Zeier, J. Janek, *Chem. Rev.* **2020**, *120*, 7745.
- [36] E. Dologlou, *Glass Phys. Chem.* **2010**, *36*, 570.
- [37] W. Weppner, R. A. Huggins, *J. Electrochem. Soc.* **1977**, *124*, 1569.
- [38] R. H. Brugge, R. J. Chater, J. A. Kilner, A. Aguadero, *J. Phys. Energy* **2021**, *3*, 034001.
- [39] S. A. Pervez, G. Kim, B. P. Vinayan, M. A. Cambaz, M. Kuenzel, M. Hekmatfar, M. Fichtner, S. Passerini, *Small* **2020**, *16*, 2000279.
- [40] Y. Wang, K. Takahashi, K. H. Lee, G. Z. Cao, *Adv. Funct. Mater.* **2006**, *16*, 1133.
- [41] J. Wu, I. Byrd, C. Jin, J. Li, H. Chen, T. Camp, R. Bujol, A. Sharma, H. Zhang, *ChemElectroChem* **2017**, *4*, 1181.
- [42] A. Priebe, L. Pethö, E. Huszar, T. Xie, I. Utke, J. Michler, *ACS Appl. Mater. Interfaces* **2021**, *13*, 15890.



## Supporting Information

for *Adv. Energy Mater.*, DOI: 10.1002/aenm.202102086

Building a Better Li-Garnet Solid Electrolyte/Metallic Li Interface with Antimony

*Romain Dubey, Jordi Sastre, Claudia Cancellieri, Faruk Okur, Alexander Forster, Lea Pompizii, Agnieszka Priebe, Yaroslav E. Romanyuk, Lars P. H. Jeurgens, Maksym V. Kovalenko,\* and Kostiantyn V. Kravchyk\**

## Supporting Information

### **Building a Better Li-Garnet Solid Electrolyte/Metallic Li Interface with Antimony**

*Romain Dubey, Jordi Sastre, Claudia Cancellieri, Faruk Okur, Alexander Forster, Lea Pompizii, Agnieszka Priebe, Yaroslav Romanyuk, Lars P.H. Jeurgens, Maksym V. Kovalenko\* and Kostiantyn V. Kravchyk\**

### Profilometry – Confirmation of Sb-Layer Thickness

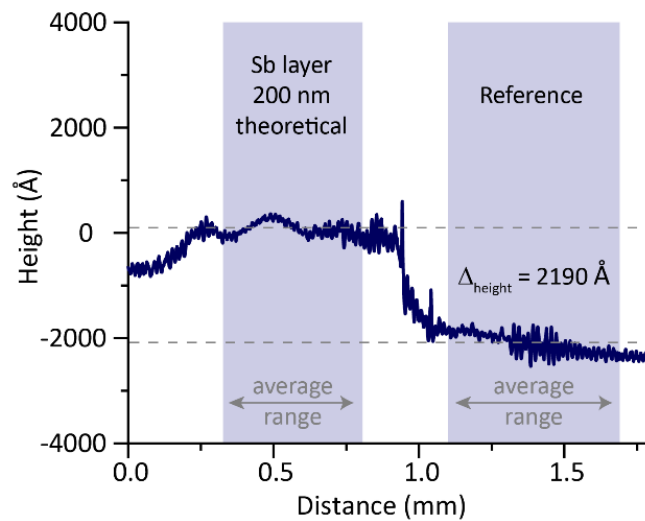


**Figure S1.** Profilometry measurements of a thick Sb layer sputtered onto a glass substrate. The data show the difference between Sb thickness (theoretical, 200 nm) determined by oscillating crystal measurements and the Sb thickness measured by profilometry (reference, 219 nm), resulting in the error of ca. 9.5%.

## XPS and HAXPES Experimental Details

XPS/HAXPES survey spectra, covering binding energy (BE) range from 0 eV to 1200 eV (0 to 5200 eV for Cr), were recorded with a step size of 0.5 eV at constant pass energy of 280 eV using the Al-K $\alpha$  source (power 51 W; beam diameter  $\sim$ 200  $\mu$ m) and the Cr-K $\alpha$  (power 100 W; beam diameter  $\sim$ 100  $\mu$ m). Composition-depth profiles were recorded by employing alternating cycles of:

- XPS analysis (Al-K $\alpha$  at 51 W; beam diameter  $\sim$ 200  $\mu$ m) and sputtering with a focused 1 keV Ar beam, rastering an area of 2 $\times$ 2 mm<sup>2</sup>.
- HAXPES analysis (Cr-K at 50.0 W; beam diameter:  $\sim$ 100  $\mu$ m) and sputtering with a focused 1 keV Ar beam, rastering an area of 2 $\times$ 2 mm<sup>2</sup>.

During each measurement cycle, the Li 1s, La 3d<sub>5/2</sub>, Zr 3p, C 1s and O 1s regions were recorded with a step size of 0.10 eV and a pass energy of 112 eV. The etch rate was calibrated to be 2.3 nm/min on a 100 nm Ta<sub>2</sub>O<sub>5</sub>/Ta reference sample.

Quantification of each element (i.e. Li, La, Zr, C, and O) was performed by constrained peak fitting of the corresponding Shirley background corrected spectra with one or more symmetrical, mixed Gaussian–Lorentzian line shape functions, using the MultiPak 9.9 software of Ulvac-Phi. The Gauss fraction of each peak component (representative of instrumental broadening) was constrained in the range of 0.8-0.9. The full width at half maximum (FWHM) and BE position of each peak component were determined from a single spectrum in the measurement series (i.e. pertaining to a given sputter cycle), which contained the highest contribution of the respective peak component. The determined FWHM and BE values for each resolved peak component (dominant at a certain sputter depth) were fixed for the batch fitting procedure of the entire spectral series (across the entire sputter depth). Atomic concentrations of the elements and the resolved chemical species were calculated from the integrated peak areas of the fitted peak components using the sensitivity

factors provided by the manufacturer (Ulvac-Phi), as derived according to ISO 18118. It is noted that LLZO is an insulator and thus experiences differential charging during XPS analysis. Charging neutralization during XPS analysis was performed using a dual-beam floodgun. No charge correction was performed to the measured data. Commonly, the adventitious carbon peak at  $283.4 \pm 0.4$  eV is charge-corrected to a reference value of 284.6 eV.

### **Depth Estimation**

XPS is a surface-sensitive analytical technique with a probing depth equal to  $3\lambda \times \sin(\theta)$ , where  $\lambda$  denotes the inelastic mean free path of the emitted photoelectrons traversing through the studied compound and  $\theta$  is the detection angle with respect to the sample surface (*here*:  $\theta = 45^\circ$ ). Values of  $\lambda$  can be calculated from the so-called TTP2 formalism adopting the density ( $5.17 \text{ g/cm}^3$ ), bandgap (6 eV) and the number of valence electrons (96) for LLZO. Notably, the relatively high surface roughness of the LLZO pellet in the range of 1-3  $\mu\text{m}$  (**Figure S3**) will lead to shadowing and roughening effects during successive cycles of sputtering and subsequent HAXPES analysis, thus deteriorating the depth resolution of the analysis.

### **Fluorine Gas-Assisted TOF-SIMS**

The Cu/Li/Sb/Al-LLZO system was characterized using the time-of-flight secondary ion mass spectrometry (TOF-SIMS) technique, which enables for 3D chemical reconstruction of a sample structure with nanoscale spatial resolution. The main advantages of this technique are parallel detection of all ionized elements and molecules (including light and heavy species) as well as recognition of isotopes. Furthermore, the TOF-SIMS measurements do not require any particular sample preparation protocols (samples should be flat and conductive), which allows the experimental time and correlated costs to be reduced. Besides, a wide range of analytical areas

(usually between 1 and  $10^4 \mu\text{m}^2$ ) provides insight into the local and global sample structure<sup>S1</sup>. In this study, a novel method<sup>S2-4</sup> of combining a HV-compatible high-resolution TOF<sup>S5,6</sup> (H-TOF) add-on from TOFWERK (Thun, Switzerland) with an *in situ* gas injection system (GIS)<sup>S7</sup> integrated within a focused ion beam/scanning electron microscope (FIB/SEM) dual-beam instrument from Tescan (Brno, Czech Republic) was used. The fluorine gas-assisted FIB-TOF-SIMS technique has been recently presented as an important technological advance due to significant enhancement of generating positive secondary ions (up to two orders of magnitude, depending on material)<sup>S2-4, 8</sup>. Consequently, a higher signal-to-noise ratio can provide increased spatial resolution and better quality of chemical images. Furthermore, it was demonstrated that simultaneous delivery of fluorine gas to a sample surface during a TOF-SIMS measurement can induce separation of mass interference<sup>S3,9</sup> (i.e. can solve one of the main drawbacks of TOF-SIMS technique under standard vacuum conditions). Finally, the initial studies seem to indicate that fluorine can alter the polarity of generated secondary ions (from negative to positive) during FIB sputtering and therefore allow for assessing directly the complete chemical structure of a sample (i.e. during one measurement, meaning exactly the same analytical volume). It is worth mentioning that TOF-SIMS is a destructive technique and without any supplementary gas, two separate measurements have to be performed to show the distribution of positively and negatively ionizing elements. The sample surface was bombarded with a continuous monoisotopic  $^{69}\text{Ga}^+$  primary ion beam (i.e. dynamic-SIMS, depth profiling mode), which was used as both, a sputtering and analysis beam. The 20 kV beam energy was used to achieve high lateral resolution whilst maintaining sufficient depth resolution. The 4D data set (i.e.  $x$ ,  $y$  and  $z$  coordinates and an associated mass spectrum for each data point), was obtained at approx.  $114 \pm 1$  pA ion current and 32  $\mu\text{s}$  dwell time from a  $10 \mu\text{m} \times 10 \mu\text{m}$  area with  $512 \times 512$  pixels and  $2 \times 2$  binning. The depth profiles were acquired from the central  $5 \mu\text{m} \times 5 \mu\text{m}$  area to prevent potential edge effect artifacts (such as material re-deposition). **Figure S4** shows a SEM image of the sample surface before and after FIB-TOF-SIMS measurements. The shape of the sputtered crater (sharp edges) indicates that no drift appeared during the measurement and that the experimental parameters (focus,  $x$ - and  $y$ -

stigmators, x- and y-beam centering) were adjusted properly. A XeF<sub>2</sub> precursor was used as a source of fluorine (i.e. the precursor molecules were defragmented with impacting Ga<sup>+</sup> ion primary beam). TOF-SIMS Explorer 1.12.2.0 from TOFWERK (Thun, Switzerland) was used for data collection and processing. Mass spectra were mass calibrated using the secondary ion signals of the main sample elements (<sup>7</sup>Li<sup>+</sup>, <sup>27</sup>Al<sup>+</sup>, <sup>63</sup>Cu<sup>+</sup>, <sup>121</sup>Sb<sup>+</sup>, <sup>139</sup>La<sup>+</sup>) and the primary ion beam (<sup>69</sup>Ga<sup>+</sup>). 3D elemental tomography plots were created using the Mayavi's mlab module for Python.

**Table S1.** Li/LLZO interfacial resistance values derived from the impedance spectra of Li/LLZO/Li symmetrical cells comprising Sb-coated LLZO pellets with different Sb thickness or heat-treated LLZO pellet without Sb.

Surface treatment	Interfacial resistance $R_{int}$ ( $\Omega \text{ cm}^2$ )
heat-treatment	28.2(1.4)
5 nm Sb	59(3)
10 nm Sb	4.1(1)
15 nm Sb	57(4)
20 nm Sb	373(7)
50 nm Sb	399(10)
100 nm Sb	660(20)

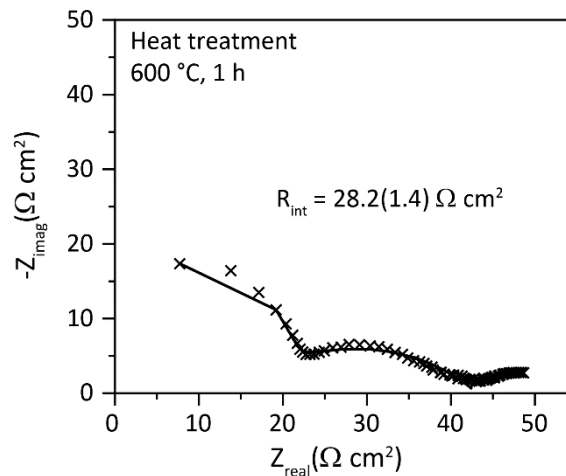


**Figure S2.** Impedance spectrum of Li/LLZO/Li symmetrical cells comprising a heat-treated LLZO pellet (600 °C for 1 h under Ar).

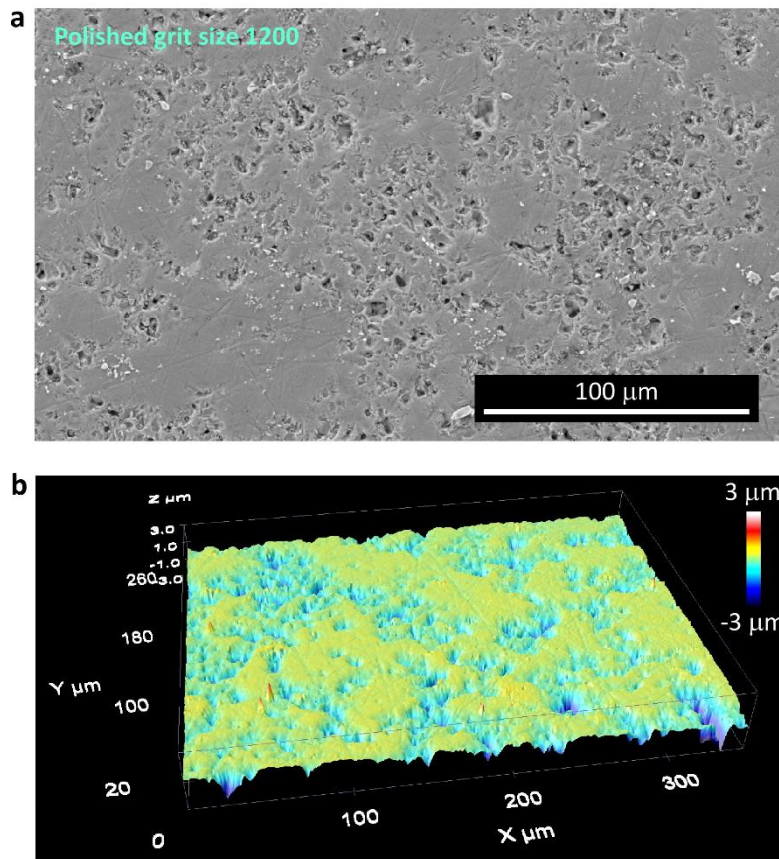


**Figure S3.** (a) SEM micrograph of a pristine, polished Al-LLZO pellet polished with SiC sandpaper with grit size 1200. (b) 3D optical surface topology measurement of the same surface performed on a 3D Optical Surface Metrology System Leica DCM8 in confocal mode.

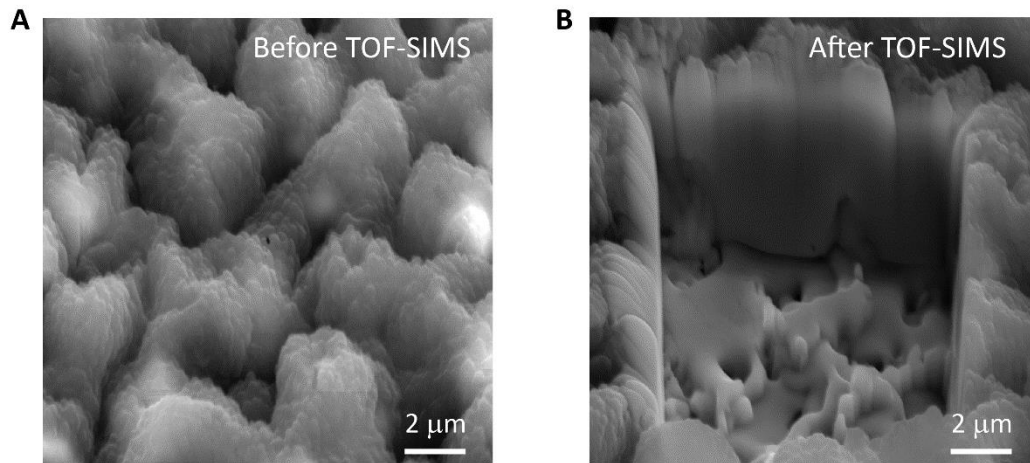


**Figure S4.** SEM images of the sample topology acquired before (A) and after (B) FIB-TOF-SIMS measurements. The high surface roughness can be the reason of detecting Sb ions across the entire sample during the chemical characterization.

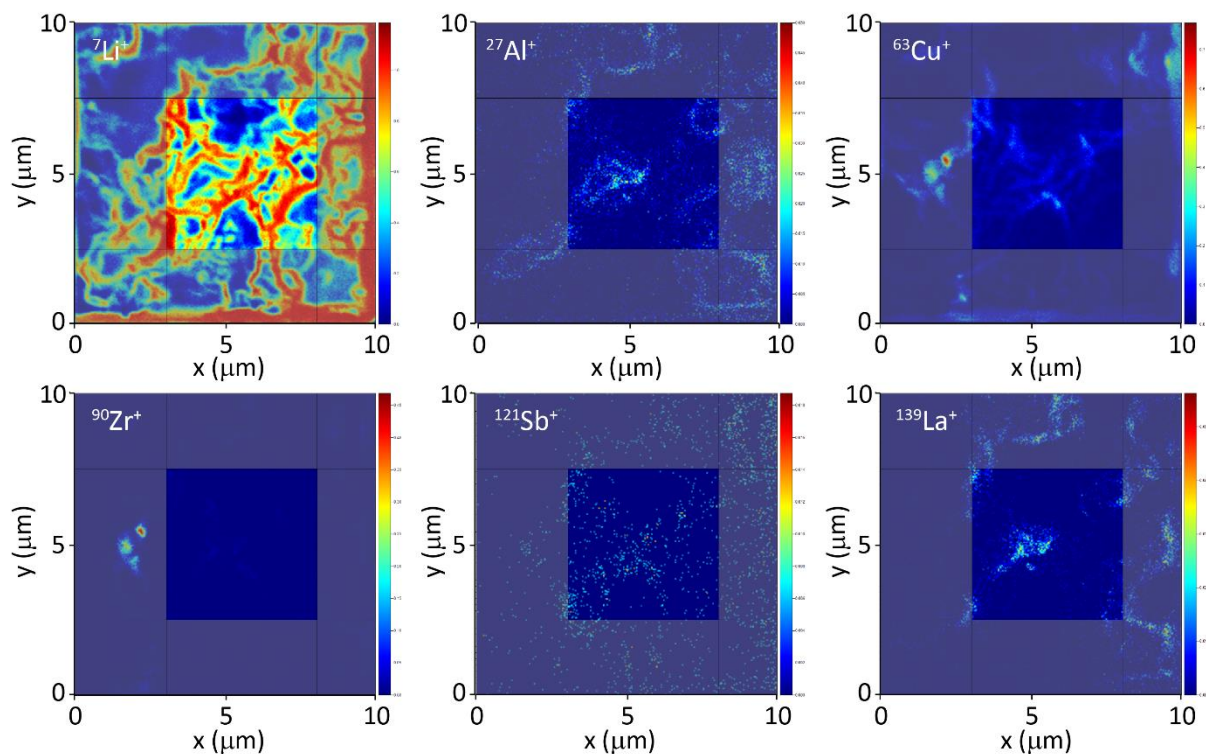


**Figure S5.** 2D chemical maps (in lateral plane) of main sample elements obtained during fluorine gas-assisted TOF-SIMS. The signal integration in z-direction over all acquired scans. Only the data from the central 5 μm × 5 μm were used for generating the depth profiles (given in Figure S5) to prevent the influence of edge effect artifacts.

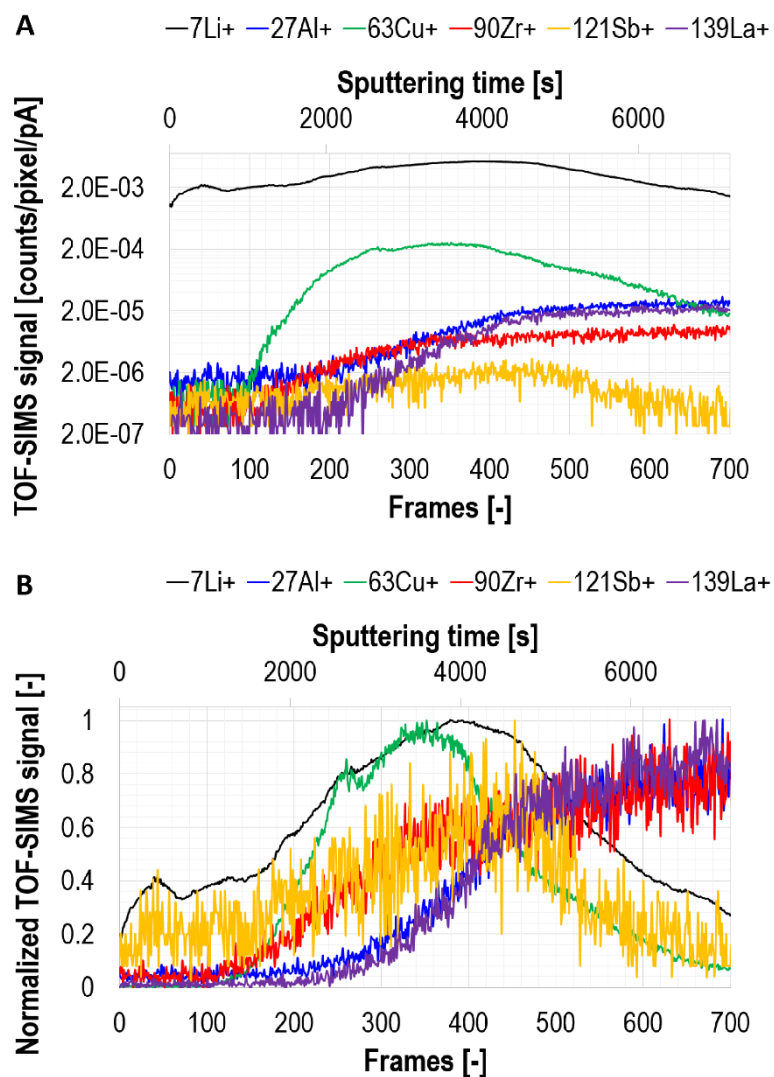


**Figure S6.** TOF-SIMS depth profiles of the sample main ion signals. **(A)** values normalized per impacting 1 pA primary ion beam, **(B)** normalized values. Signal integration in x-y plane. Note that the z-dimension is given as a number of frames (i.e. acquisition scans) and sputtering time as it is not possible to assess the thickness of the sputtered material directly from the TOF-SIMS measurements (unless the sputtering rates are known, which is usually not the case for novel materials measured under optimized primary ion beam parameters).

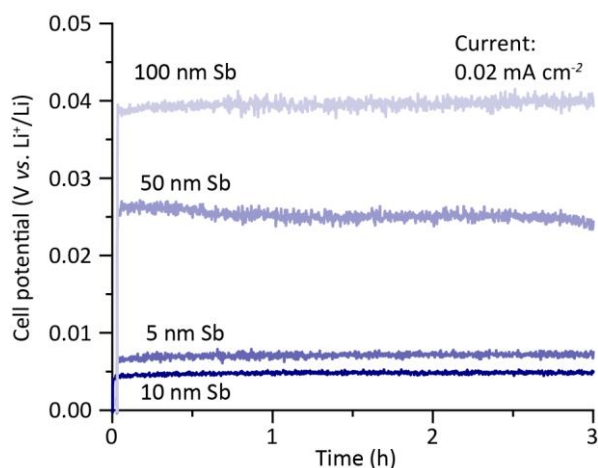


**Figure S7.** Comparison of initial voltage profiles of Li/Sb-coated LLZO/Li symmetrical cells comprising Sb-coated LLZO pellets with different Sb thickness (5, 10, 50 and 100 nm). The measurements were performed at current densities of  $0.02 \text{ mA cm}^{-2}$ .

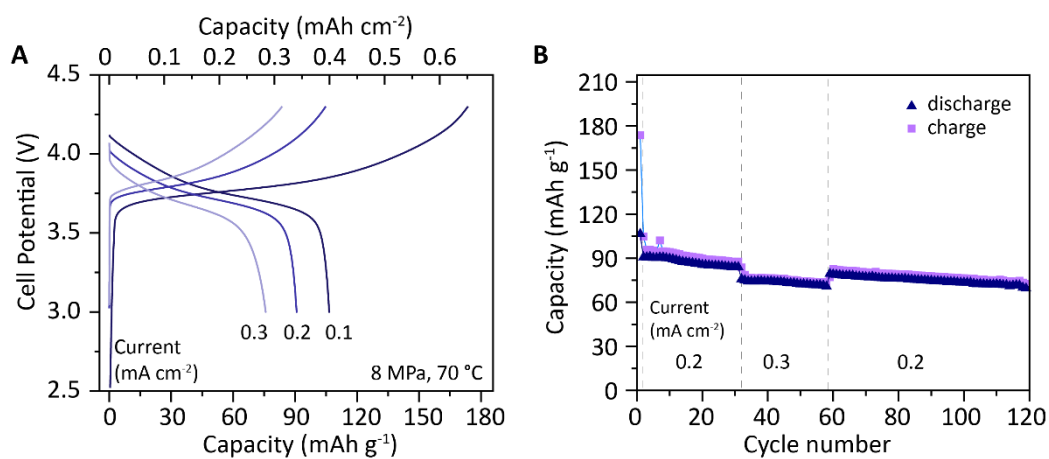


**Figure S8.** (a) Typical galvanostatic charge-discharge voltage profiles and (b) cyclic stability measurements of NMC532|Sb-coated-LLZO|Li full cell at current densities of 0.1, 0.2 and  $0.3 \text{ mA cm}^{-2}$ .

## References

1. A. Priebe, J.-P. Barnes, T. E. J. Edwards, E. Huszár, L. Pethö and J. Michler, *Analytical Chemistry*, 2020, **92**, 12518-12527.
2. A. Priebe, I. Utke, L. Pethö and J. Michler, *Analytical Chemistry*, 2019, **91**, 11712-11722.
3. A. Priebe, L. Pethö and J. Michler, *Analytical Chemistry*, 2020, **92**, 2121-2129.
4. A. Priebe, T. Xie, L. Pethö and J. Michler, *Journal of Analytical Atomic Spectrometry*, 2020, **35**, 2997-3006.
5. J. A. Whitby, F. Östlund, P. Horvath, M. Gabureac, J. L. Riesterer, I. Utke, M. Hohl, L. Sedláček, J. Jiruše, V. Friedli, M. Bechelany and J. Michler, *Advances in Materials Science and Engineering*, 2012, **2012**, 180437.
6. D. Alberts, L. von Werra, F. Oestlund, U. Rohner, M. Hohl, J. Michler and J. A. Whitby, *Instrumentation Science & Technology*, 2014, **42**, 432-445.
7. Z. M. Wang, *FIB Nanostructures*, Springer International Publishing, 2012.
8. A. Priebe, L. Pethö, E. Huszar, T. Xie, I. Utke and J. Michler, *ACS Applied Materials & Interfaces*, 2021, **13**, 15890-15900.
9. A. Priebe, E. Huszar, M. Nowicki, L. Petho and J. Michler, *Anal. Chem.*, 2021, **93**, 10261.